OPTICAL SCATTERING BASED RANDOM FOREST ASSISTED PARTICLE DETECTION AND CLASSIFICATION

A THESIS
SUBMITTED TO
THE DEPARTMENT OF
ELECTRICAL AND COMPUTER ENGINEERING AND
THE GRADUATE SCHOOL OF ENGINEERING & SCIENCE OF
ABDULLAH GÜL UNIVERSITY
IN PARTIAL FULFILLMENT OF THE REQUIREMENTS
FOR THE DEGREE OF
Ph.D.

By
Sinan GENÇ
July 2023

OPTICAL SCATTERING BASED
RANDOM FOREST ASSISTED
PARTICLE DETECTION AND CLASSIFICATION

A THESIS
SUBMITTED TO
THE DEPARTMENT OF
ELECTRICAL AND COMPUTER ENGINEERING AND
THE GRADUATE SCHOOL OF ENGINEERING & SCIENCE OF
ABDULLAH GÜL UNIVERSITY
IN PARTIAL FULFILLMENT OF THE REQUIREMENTS
FOR THE DEGREE OF
Ph.D.

By
Sinan GENÇ
July 2023

SCIENTIFIC ETHICS COMPLIANCE

I hereby declare that all information in this document has been obtained in accordance with academic rules and ethical conduct. I also declare that, as required by these rules and conduct, I have fully cited and referenced all materials and results that are not original to this work.

Sinan GENÇ

REGULATORY COMPLIANCE

Ph.D. thesis titled "Optical Scattering Based Random Forest Assisted Particle Detection and Classification" has been prepared in accordance with the Thesis Writing Guidelines of the Abdullah Gül University, Graduate School of Engineering & Science.

Prepared By	Advisor	Co-Advisor
Sinan GENÇ	Assoc. Prof.	Assist. Prof.
	Kutay İÇÖZ	Talha ERDEM

Head of the Electrical and Computer Engineering Program
Assoc. Prof. Zafer AYDIN

ACCEPTANCE AND APPROVAL

Ph.D. thesis titled "**Optical Scattering Based Random Forest Assisted Particle Detection and Classification**" and prepared by Sinan Genç has been accepted by the jury in the Electrical and Computer Engineering Graduate Program at Abdullah Gül University, Graduate School of Engineering & Science.

13/07/2023

JURY:

Advisor : Assoc. Prof. Kutay İÇÖZ

Member : Prof. Mehmet ŞAHİN

Member : Assist. Prof. Dooyoung HAH

Member : Prof. Hümeyra ÇAĞLAYAN

Member : Assoc. Prof. İbrahim Tuna ÖZDÜR

APPROVAL:

The acceptance of this Ph.D. thesis has been approved by the decision of the Abdullah Gül University, Graduate School of Engineering & Science, Executive Board dated ….. /….. / ……….. and numbered …………..……… .

…. /….. / …..

Graduate School Dean
Prof. İrfan ALAN

ABSTRACT

OPTICAL SCATTERING BASED RANDOM FOREST ASSISTED PARTICLE DETECTION AND CLASSIFICATION

Sinan GENÇ
Ph.D. in Electrical and Computer Engineering
Advisor: Assoc. Prof. Kutay İÇÖZ
Co-Advisor: Assist. Prof. Talha ERDEM
July 2023

Microplastics, tiny plastic particles with sizes smaller than 5 mm., are often found in oceans, rivers, lakes, and atmosphere due to plastic pollution. Microplastics releasing toxic chemicals threaten the environment and harm the aquatic life and humans. Especially, the accumulation of microplastics can have detrimental effects on the food chain as a result of larger organisms consuming smaller organisms.

Detecting the microplastics is crucial but also challenging. Over the years, researchers have developed different detection methods. One of the standard methods is using spectroscopy tools such as Fourier transform infrared spectroscopy (FTIR) and Raman spectroscopy. These techniques can identify the chemical composition of microplastics, which can help determine their sources and potential impacts. Another method is the use of microscopy, which allows for the visualization and counting of microplastics in samples. However, these techniques require costly infrastructure, and these instruments being large in size significantly limits the mobility.

As a remedy to the cost and mobility problems, in this thesis, we propose and demonstrate a low-cost, portable system to detect size, concentration, and refractive index of microplastics. Our system comprises of low-cost and low-weight components which are utilized for recording the scattering patterns of microplastics in aqueous media. We demonstrate successful predictions of the size and refractive index of microparticles at a given wavelength using a Random Forest Algorithm which relates the measured scattering pattern with the Mie theory. We further employ the refractive index information at various wavelengths for determining the material type of microplastics.

We believe that our proposed system enabling an easy, fast, low-cost, and on-site detection of microplastics will be a beneficial tool for the fight against microplastics in the environment.

Keywords: scattering, optics, sensing, microparticle, machine learning.

ÖZET

OPTİK SAÇILMA TEMELLİ RASTGELE ORMAN DESTEKLİ PARÇACIK TESPİTİ VE SINIFLANDIRILMASI

Sinan GENÇ
Elektrik ve Bilgisayar Mühendisliği Anabilim Dalı Doktora
Danışman: Doç. Dr. Kutay İÇÖZ
İkinci Danışman: Dr. Öğr. Üyesi Talha ERDEM
Haziran 2023

5 mm'den küçük boyutlara sahip küçük plastik parçacıklar olan mikroplastikler, plastik kirliliği nedeniyle genellikle okyanuslarda, nehirlerde, göllerde ve atmosferde bulunur. Zehirli kimyasallar salan mikroplastikler çevreyi tehdit etmekte, su canlılarına ve insanlara zarar vermektedir. Özellikle yayılmaları ve daha büyük organizmaların daha küçük organizmaları tüketmesi sonucunda besin zinciri üzerinde zararlı olabilirler.

Mikroplastikleri tespit etmek çok önemli ama aynı zamanda zordur. Yıllar boyunca, araştırmacılar farklı tespit yöntemleri geliştirmişlerdir. Standart yöntemlerden biri, Fourier dönüşümü kızılötesi spektroskopisi (FTIR) ve Raman spektroskopisi gibi spektroskopi araçlarını kullanmaktır. Bu teknikler, mikroplastiklerin kaynaklarını ve potansiyel etkilerini belirlemeye yardımcı olabilecek kimyasal bileşimini tanımlayabilir. Diğer bir yöntem ise numunelerdeki mikroplastiklerin görselleştirilmesine ve sayılmasına izin veren mikroskopi kullanımıdır. Ancak bu teknikler maliyetli altyapı gerektirir ve bu enstrümanların boyutlarının büyük olması taşınabilirliği önemli ölçüde sınırlar.

Maliyet ve taşınabilirlik sorunlarına bir çözüm olarak, bu tezde, mikroplastiklerin boyutunu, konsantrasyonunu ve kırılma indeksini tespit etmek için düşük maliyetli, taşınabilir bir sistem öneriyor ve sunuyoruz. Sistemimiz, mikroplastiklerin sulu ortamdaki saçılma modellerini kaydetmek için düşük maliyetli ve düşük ağırlıklı bileşenlerden oluşur. Ölçülen saçılma modelini Mie teorisi ile ilişkilendiren bir Rastgele Orman Algoritması kullanarak, belirli bir dalga boyunda mikropartiküllerin boyutuna ve kırılma indisine ilişkin başarılı tahminler gösteriyoruz. Ayrıca, mikroplastiklerin malzemesini belirlemek için çeşitli dalga boylarındaki kırılma indislerini de kullanıyoruz.

Mikroplastiklerin kolay, hızlı, düşük maliyetli ve yerinde tespit edilmesini sağlayan önerdiğimiz sistemimizin, çevredeki mikroplastiklerle mücadelede faydalı bir araç olacağına inanıyoruz.

Anahtar kelimeler: saçılma, optik, algılama, mikro-parçacık, makina öğrenmesi.

Acknowledgments

TABLE OF CONTENTS

LIST OF FIGURES

LIST OF TABLES

LIST OF ABBREVIATIONS

DLS	Dynamic light scattering
FTIR	Fourier-transform infrared spectroscopy
MALS	Multi-angle light scattering
Me	Melamine
PS	Polystyrene
SDG	Sustainable development goal
SEM	Scanning electron microscopy
SLS	Static light scattering
UPW	Ultra-pure water
UV	Ultraviolet

"To infinity and beyond!"

Chapter 1

Introduction

1.1 Microplastic Pollution

Microplastics are tiny pieces of plastics smaller than 5 mm in size. They come from various sources, such as broken-down plastic waste, microbeads from personal care products, synthetic fibers from textiles, and through fragmentation of larger plastic debris [1–3]. Microplastics pose a significant threat to marine and freshwater ecosystems as they are frequently ingested by aquatic life and can accumulate in the food chain, ultimately reaching humans [4–9]. As given in Figure 1.1, micrometer-sized living beings in the oceans have plastics in their body. Other life forms, which are at higher places in the food chain, consume them leading the micropollutants eventually to reach the human body.
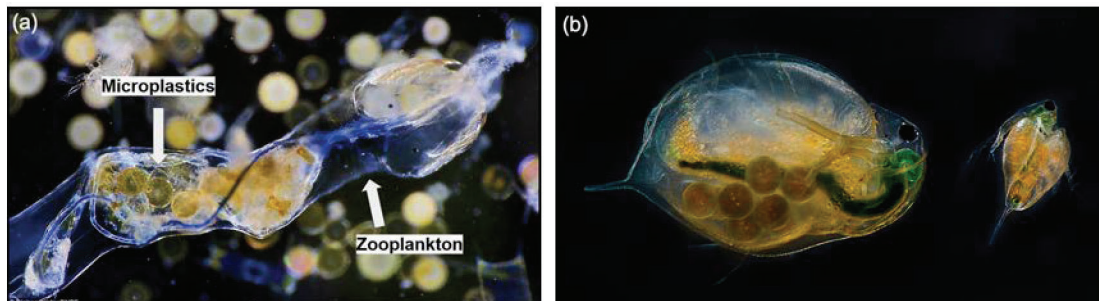
Figure 1.1 (a) A zooplankton (2-20 µm) [10] (This image was reproduced with permission of Dr. Richard Kirby), and (b) a water flea (200+ µm) [11] with microplastics in their body.

Plastics from automobile tires, industry, and other resources increased the amount of those pollutants in addition to this aquatic connection [12–16]. Recent scientific studies have demonstrated the presence of these tiny particles in the bodies, blood, milk, and flesh of farm animals, as well as in food products, including honey, sugar, salt, and seafood.

Another study indicated that micro/nanosized submerged plastics rise to the surface of the water resources and mix with the air due to evaporation [17]. Rains return those microplastics in the air to earth and make them in contact with land. Thus, interaction with the same pollutants again and again becomes inevitable. In addition to the food chain,

inhaling microplastics is another dangerous mechanism for human health. The danger of breathing in microplastics grows with decreasing their sizes [18]. As shown in Figure 1.2 demonstrating a sample cycle of microplastic pollution, pollutants from daily activities reach the water sources, seas, and oceans. Mechanical, biological, or natural processes make them smaller and complete the cycle with seafood, atmosphere, or direct water consumption.
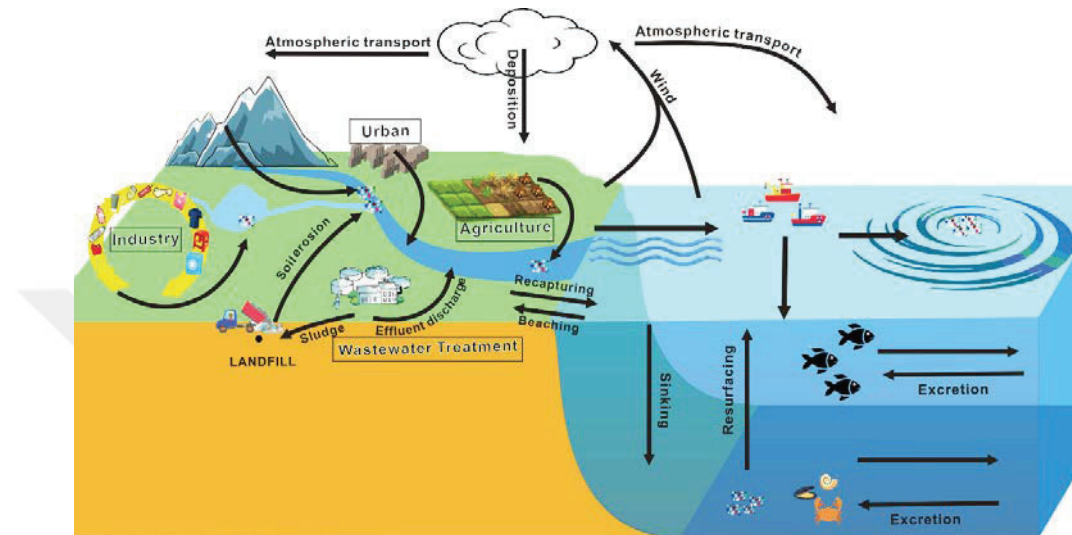
Figure 1.2 A sample microplastic pollution cycle example [19].

The environmental impacts of microplastics are still not completely understood, but they have been linked to health problems in marine life, such as reproductive issues, behavioral changes, and death. In addition, microplastics can also have economic impacts on the fishing and tourism industries, as the presence of plastics in water can reduce fish populations and lead to beach closures [20].

The issue of microplastics has gained attention in recent years due to the increasing amount of plastic waste produced globally [21–24]. Plastic is cheap, versatile, and durable, but it is also non-biodegradable, and as a result, it remains in the environment for centuries. To protect the health and environment, it is crucial to reduce the use of plastics and increase awareness on this global issue.

Recent years have seen an increase in research on microplastic pollution, with numerous studies highlighting the extent of the problem. In 2018, a study estimated that microplastics were present in more than 90% of bottled water, with an average of 325 particles per liter [25]. Another study published in 2020 estimated that up to 14 million metric tons of microplastics were deposited in the world's oceans yearly, with the majority originating from Asia [26]. Additionally, a study published in 2023 found that microplastics were present in more than 90% of the freshwater samples collected from

the Amazon and its tributaries [27]. These findings highlight the urgent need to address the root causes of microplastic pollution and prevent further harm to our environment and health.

Figure 1.3 Sample map for microplastics and their detected locations around the world (This image was reproduced with permission of planetcare.org) [28].

As microplastics are small, it is difficult to remove them from the environment once they have been released, and current recycling efforts are ineffective in eliminating them. In Figure 1.3, some of the microplastics and their locations are presented; as can be understood, they are in everywhere. Therefore, the best way to prevent microplastics is to eliminate them before dissipation. Some measures to address the problem include introducing legislation to ban microbeads in personal care products, promoting sustainable alternatives, and increasing investment in research to better understand the impacts of microplastics on the environment and human health.

1.2 Detection of Microplastics

As microplastics continue to pose a significant problem due to their evasive nature and ineffective recycling techniques, the need for proactive measures to prevent their release grows. Efforts are being made to implement practical solutions in response to the widespread distribution of microplastics. The application of optical scattering techniques for detecting microplastics is among them. This novel technique employs light scattering to identify and quantify microplastic particles within a sample. It capitalizes on their

unique ability to scatter light at certain angles depending on the size and type of microparticles. By utilizing this innovative method, researchers can obtain valuable insights into the prevalence and distribution of microplastics, which will ultimately aid in developing effective strategies to combat their environmental impact and protect the ecosystem and human health.

Microplastic detection by optical scattering is a technique that uses light scattering to identify and quantify microplastic particles in a sample. The method relies on the fact that microplastics are usually small enough to scatter light at a particular angle, distinguishing them from other particles in the sample.

To detect microplastics by optical scattering, a sample is first prepared by filtering it through a fine mesh or membrane to remove larger particles. The filtered sample is then passed through a laser beam or other light source at a specific angle to the sample. As the light passes through the sample, it interacts with any microplastic particles present, causing them to scatter light at a particular angle. A detector is positioned to capture this scattered light, which can then be analyzed to identify and quantify the microplastics in the sample.

One advantage of this technique is that it is non-destructive and non-invasive, meaning that the sample can be preserved for further analysis. Additionally, it can be performed relatively quickly and requires minimal sample preparation.

However, microplastic detection by optical scattering possess some limitations. For example, it may not be able to detect very small microplastics or those that have refractive indices similar to water leading to a transparent or translucent appearance. In addition, other particles in the sample may also scatter light, making it challenging to distinguish microplastics from other particles. Therefore, it is often used in combination with other analytical techniques, such as microscopy or spectroscopy, to provide a more complete picture of the microplastics present in a sample.

Several optical techniques can detect microplastics in various media such as sediment, soil, and air. Within the framework of this thesis, optical techniques can be used to determine microplastics in liquids, such as water, by either visualizing the microplastics directly or indirectly detecting them through their interaction with light. Some of the most commonly used optical techniques for determining microplastics are shortly defined as follows:

Microscopy: Microscopy techniques, such as brightfield, darkfield, and phase contrast microscopy, can be used to visualize microplastics in liquid samples directly [29].

Fluorescence microscopy: This technique involves labeling microplastics with a fluorescent dye and then visualizing them under a microscope with a UV light source [30]. The microplastics appear as bright fluorescent particles against a dark background, making them easy to detect and quantify.

Digital holographic microscopy: Digital holographic microscopy involves recording interference patterns generated by a laser beam that has passed through a sample [31]. This technique can detect and characterize microplastics based on their 3D morphology and optical properties.

Fourier-transform infrared (FTIR) spectroscopy: FTIR spectroscopy measures a sample's absorption or transmission of infrared light [32]. Different types of plastic have unique infrared spectra, which can be used to identify and quantify microplastics.

Flow cytometry: Flow cytometry can quantify and size particles in a liquid sample [33]. Microplastics can be labeled with a fluorescent dye and then analyzed by flow cytometry to determine their concentration and size distribution.

Infrared spectroscopy: Infrared spectroscopy can identify and quantify microplastics in liquid samples by measuring their characteristic absorption or transmission of infrared light [34].

Raman spectroscopy: Raman spectroscopy is a non-destructive technique involving a laser on a sample and measuring the scattered light [35]. Each type of plastic has a unique Raman spectrum, which can be used to identify and quantify different types of microplastics.

Surface plasmon resonance imaging: Surface plasmon resonance imaging can detect and quantify microplastics in liquid samples based on their interaction with a metallic surface [36]. The presence of microplastics in the liquid sample causes changes in the refractive index of the surrounding medium, which can be detected by surface plasmon resonance imaging.

Hyperspectral imaging: Hyperspectral imaging involves collecting images at multiple wavelengths across the electromagnetic spectrum, allowing for the identification and characterization of microplastics based on their spectral signatures [37].

Overall, optical techniques provide powerful tools for detecting and characterizing microplastics in various environmental samples and can generate essential data for

monitoring and mitigating microplastic pollution. However, these systems are usually bulky and costly, making it inaccessible and difficult for on-site use. As an alternative to the existing techniques, here we propose and demonstrate a simple, cost-effective, and fast-response technique to determine particle size, refractive index, and concentration of microparticles in water. Our system includes several low-power lasers, a sample holder, screen and a Raspberry Pi card equipped with a camera. By recording the scattering patterns of the laser light and subsequently relating it with the Mie theory with the help of Random Forest Algorithm, we successfully determined the concentration, type, and size of the particles.

1.3 Contributions and Structure of Thesis

In literature, there are studies determining the size of microparticles regardless of the material type [35,38–41]. Although it is easier to classify particles of various sizes, the situation would be tricky if the particles were identical in every aspect except the materials they are made of. In this thesis, in addition to the particle size, concentration, and wavelength of incident light, the materials of particles are also examined, and classification by random forest algorithm is presented. Distinguishing the particle will open a new window to classify microplastic pollution and its hazard level. Furthermore, it would be possible to track the path of microplastics starting from the source.

In the first experiments, as presented in Figure 1.4 by unprofessional photos taken using a mobile phone camera, it was observed that a low-cost setup could show different scattering patterns for particles of various sizes, refractive index, concentration, and wavelength of incident lights.
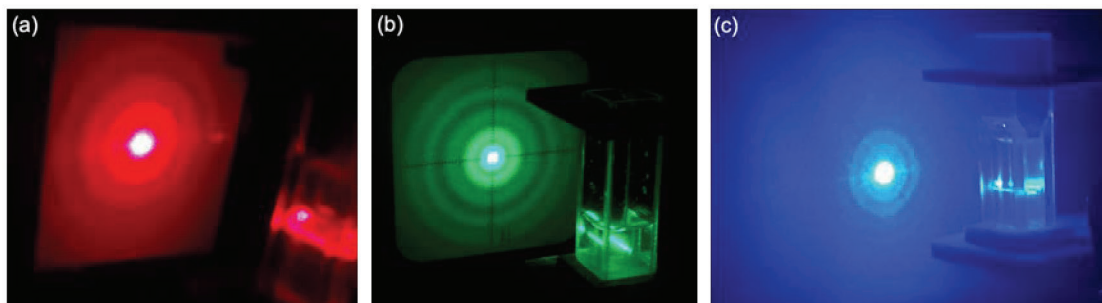
Figure 1.4 Mobile phone shootings showing different scattering patterns for red (a), green (b), and blue (c) laser light, meaning that the proposed low-cost setup would provide information for classification.

After having promising data from the first observation, we analyzed the effects of particle size, refractive index, concentration, and wavelength of incident light on scattering patterns for samples consisting of melamine and polystyrene particles.

Mixing the samples given in previous parts with a known percentage and investigating the mixtures' scattering patterns are further steps of this study. Having two different microplastics in one sample affects the scattering patterns due to different refractive indices or sizes or concentrations of those microparticles. In this part, the relation between the individual scattering data of these particles and their combinations will be presented.

If a water sample contains two different sizes of microplastics, their behavior and interactions can be more complex than the samples composed of same-sized particles. The coexistence of multiple microplastic sizes can have various implications for their dispersion, settling, and potential impacts on the environment [42] Larger particles would have a tendency to settle fast compared to the small ones and they would hit the small ones. This would have a change in settlement behavior of small particles in the mixture. Although particles with bigger sizes would be easy to filter or eliminate by membranes, if there are smaller ones in the same sample, they may continue to threaten the environment.

Some key considerations when two different sizes of microplastics are present in a sample:

Settling and Suspension: Larger microplastics are generally more likely to settle out of the water column due to their greater mass and sedimentation rates. On the other hand, smaller microplastics may remain suspended in the water for more extended periods. This difference in behavior can lead to spatial and temporal variations in microplastic distribution.

Aggregation: Microplastics of different sizes may have different surface properties and charges, which can influence their tendency to aggregate with each other or other particles in the water. Aggregation can affect the overall size and buoyancy of the microplastic particles.

Transport: Microplastics of different sizes may be transported differently by water currents. For example, larger microplastics may be more affected by currents closer to the water surface, while smaller ones could be dispersed more broadly in the water column.

Sampling and Analysis: Multiple microplastic sizes can complicate sampling and analysis procedures. Researchers may need specialized techniques to distinguish and quantify the different sizes accurately.

Ecological Impacts: Different sizes of microplastics may pose different risks to aquatic organisms. Some species might readily ingest specific size ranges, leading to varied environmental impacts.

Researchers conduct studies considering size distribution and concentration data to comprehensively understand the effects of multiple microplastic sizes in a water sample. Analyzing samples through microscopy, spectroscopy, or imaging can provide valuable insights into the behavior and potential impacts of different microplastic sizes in aquatic environments.

It is crucial to continue researching and monitoring microplastics in water and water related environments i.e., marine life, to understand their behavior and potential environmental and human health consequences better. Determining the concentration of two different microplastics of varying sizes in an aqueous sample requires careful laboratory analysis. Several methods are commonly used to measure microplastic concentrations, each with advantages and limitations. A general outline of steps to determine the concentration of two different microplastics at different sizes [43–45]:

Sample Collection: Collect water samples from the target location using appropriate sampling techniques and equipment. Ensure that the samples are handled carefully to avoid contamination.

Sample Preparation: Depending on the analysis method, you may need to concentrate the microplastics from the water sample. This can be done through filtration, centrifugation, or density separation methods.

Microplastic Extraction: Extract the microplastics from the concentrated sample using suitable chemical or physical methods. Typical approaches involve using chemical solutions to digest organic matter or floatation in saline solutions.

Microscopy: Use microscopy to identify and count the microplastics visually. For this, you'll need to prepare slides or filters with the extracted microplastics and use a microscope to examine and identify them. Different stains or dyes may be used to enhance the visibility and differentiation of microplastics.

Particle Sizing: Measure the size of individual microplastic particles using image analysis software or other particle sizing techniques. This step is essential to differentiate two types of microplastics present in the sample.

Quantification: Count and quantify the number of microplastics of each size category. The concentration can be expressed as the number of microplastics per unit volume (e.g., particles per liter) or per unit weight of sediment (e.g., particles per gram).

Chemical Analysis (Optional): Depending on the research objectives, one should characterize the composition of the microplastics (e.g., polymer type) using Fourier-transform infrared spectroscopy (FTIR) or Raman spectroscopy.

Quality Control: Implement quality control measures throughout the analysis to ensure the accuracy and reliability of the results. This may involve using blank controls to check for contamination and repeating the analysis for validation.

Choosing appropriate methods and conducting the analysis precisely is essential, as microplastics can be challenging to distinguish from natural particles or artifacts during microscopy. Researchers often use multiple techniques and replicate the analysis to ensure robust results.

The selection of specific methods and protocols can vary depending on the research objectives, available resources, and the level of sensitivity required for detection. Consulting scientific literature and established protocols is crucial when conducting such analyses.

Using scattering techniques to determine the concentration of different microplastic sizes in a water sample is innovative. Scattering refers to the interaction of light with particles, and it has been widely used in various fields, including environmental science and particle analysis [46–48]. However, applying scattering for microplastic analysis comes with specific challenges and considerations:

Scattering Theory: Scattering measurements can provide valuable information about the size, shape, and optical properties of particles, including microplastics. However, interpreting the scattering data to determine the concentration of specific microplastic sizes requires calibration and validation against known standards or well-established models.

Polydispersity: In natural samples, microplastics are often polydisperse, meaning that they come in a range of sizes rather than a single size. Scattering techniques need to account for this polydispersity to accurately assess the presence and concentration of different microplastic size classes.

Sample Complexity: Water samples contain various other particles and dissolved substances that can also contribute to scattering signals. Careful sample preparation and data analysis are necessary to isolate the scattering signals from microplastics.

Scattering Geometry: The scattering properties of microplastics depend on the angle and wavelength of incident light and the scattering angle. Determining the optimal scattering geometry for accurate measurement is critical.

Instrumentation: Scattering analysis requires specialized instruments, such as laser diffraction analyzers or dynamic light scattering (DLS) devices, which may only be available in some laboratories.

Sensitivity and Detection Limit: The sensitivity of the scattering technique must be sufficient to detect the relatively small microplastic particles in environmental samples. Additionally, the detection limit should be carefully determined to avoid false negatives.

Validation: As with any analytical method, validation of the scattering approach against reference methods (e.g., microscopy) and known microplastic standards is crucial to ensure accuracy and reliability.

While scattering techniques offer the potential for non-destructive and rapid analysis, they may still need to be more widely adopted for microplastic study as other more established methods like microscopy and spectroscopy. Researchers continuously explore and develop innovative approaches to enhance microplastic detection and characterization.

In this thesis, the theory of scattering, derivation of equations, and proposed system are given in Chapter 2. Then, Chapter 3 explains the experimental setup, samples, image processing, and machine learning steps. Chapter 4 includes the effect of parameters, i.e., concentration, particle size, particle refractive index, and wavelength of incident light, on scattering. Machine learning integration and results are given in Chapter 5. The thesis finishes with Chapter 6, conclusions, prospects, and societal and sustainable contributions.

Chapter 2

Background

2.1 How to Measure Scattering?

Scattering theory is a fundamental concept in physics that describes the behavior of waves and particles when they interact with a potential or an obstacle. It provides a mathematical framework to calculate the probability of a particle being scattered in a particular direction, as well as the phase shift of the scattered wave. It has applications in various fields, including nuclear physics, solid-state physics, astrophysics, and even medical imaging. In this context, understanding scattering theory is essential for anyone interested in exploring the behavior of waves and particles at the microscopic level.

There are several types of scattering, each characterized by the nature of the incident wave and the target or scatterer involved. The most common types of scattering include:

Rayleigh Scattering: This type of scattering occurs when electromagnetic radiation, such as visible light or radio waves, interacts with particles much smaller than the wavelength of the radiation [49]. Rayleigh scattering is responsible for the blue color of the sky, as well as the reddening of the sun at sunset.

Mie Scattering: Mie scattering occurs when electromagnetic radiation interacts with particles comparable in size to the wavelength of the radiation [50]. This type of scattering is responsible for the white color of clouds, as well as the colors of certain gemstones.
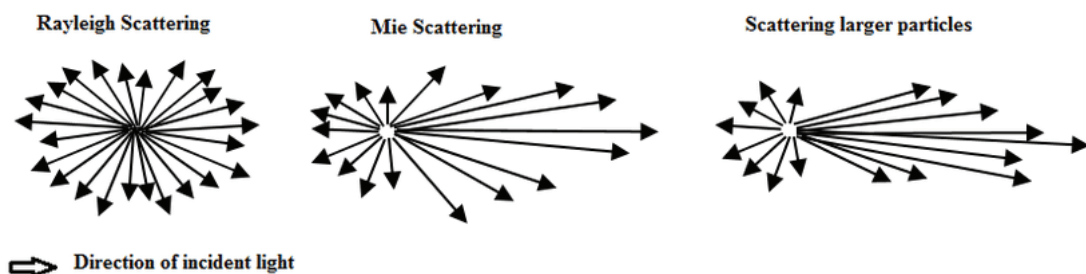
Figure 2.1 Optical scattering intensity levels at different angles dependent on particle size.

As presented in Figure 2.1, forward scattering becomes dominant when particle size increases [51]. Scattered light at lower degrees gets closer to zero-degree, making a brighter and smaller spot on the screen.

Compton Scattering: Compton scattering occurs when high-energy photons, such as X-rays or gamma rays, collide with charged particles, such as electrons [52]. During this process, the photon loses energy and momentum while experiencing changes in the propagation direction.

Rutherford Scattering: Rutherford scattering occurs when charged particles, such as alpha particles, interact with the nucleus of an atom [53]. During this process, the trajectory of the charged particle is deflected due to the electrostatic repulsion between the two charged particles.

Elastic Scattering: Elastic scattering occurs when the energy and momentum of the incident particle are conserved during the scattering process [54]. This type of scattering is characterized by a change in the direction of the incident particle without any change in its energy or wavelength.

Inelastic Scattering: Inelastic scattering occurs when the energy and momentum of the incident particle are not conserved during the scattering process [55]. This type of scattering is characterized by a change in energy, wavelength, or both.

Scattering theory can be used to detect and characterize microplastics in water by analyzing how light scatters off the particles. When light passes through a medium, such as water, it interacts with particles in the medium, causing it to scatter in different directions. The scattered light can be measured and analyzed to determine the size and concentration of the particles in the medium. Scattering theory can be used in several ways to detect microplastics in water:

Dynamic Light Scattering (DLS): DLS is a technique that measures the intensity and time dependence of scattered light from particles in a liquid to determine their size distribution [56]. Their size distribution can be determined by analyzing the scattered light from microplastics as a function of time by relating these measurements to Brownian motion.

Static Light Scattering (SLS): SLS is a technique that measures the intensity of scattered light from a sample of known concentration and compares it to a standard curve to determine the concentration of the particles in the sample [57]. This technique can be used to quantify the concentration of microplastics in water.

Multi-Angle Light Scattering (MALS): MALS is a technique that measures the intensity of scattered light from a sample at different angles to determine the size distribution and concentration of the particles in the sample [58]. This technique can determine the size and concentration of microplastics in water.

In this study, after investigation of settlement and having the same scattering angles for different concentrations, we assume that the movement of particles does not affect experiments. Therefore, minor effects of DLS can be ignored, and the system can be considered as an SLS concept.

2.2 Derivation of Mie Theory

The development of Mie theory is a significant milestone in the understanding of light scattering by particles. Mie scattering theory is a theoretical framework that describes the scattering of electromagnetic radiation by particles comparable in size to the wavelength of the radiation. This type of scattering is named after the German physicist Gustav Mie, who first developed the theory in 1908. The Mie theory is an extension of Rayleigh scattering theory, which is valid for particles much smaller than the wavelength of the radiation. It is particularly relevant in the study of atmospheric and oceanic optics, as well as in the field of materials science.

Mie theory provided a rigorous theoretical framework for calculating the scattering and absorption of light by spherical particles of different sizes and refractive indices, irrespective of the size of the particles compared to the wavelength of incident light.

Before Mie's work, a more straightforward scattering theory, known as the Lorenz-Mie theory, was developed independently by Hendrik Lorentz and Gustav Mie's colleague, Arnold Sommerfeld [50,59,60]. This theory addressed the scattering of electromagnetic waves by a dielectric sphere and provided solutions for the case of Rayleigh scattering (when the particle size is much smaller than the wavelength) and geometrical optics (when the particle size is much larger than the wavelength). However, the Lorenz-Mie theory lacks a complete solution for particles of intermediate sizes.

Gustav Mie, inspired by the work of Lorenz and Sommerfeld, expanded the theoretical framework and found exact solutions for the scattering of light by spherical particles of any size and refractive index. His approach used spherical harmonics and Bessel functions to solve Maxwell's equations for light scattering from a sphere [49,60,61]. The resulting solution, now known as Mie theory, provided a complete

description of light scattering by particles with sizes comparable to the wavelength of light.

Mie's seminal work, "Beiträge zur Optik trüber Medien, speziell kolloidaler Metallösungen" (Contributions to the optics of turbid media, specifically colloidal metal solutions), was published in 1908 [62,63]. In this work, Mie presented the complete mathematical formalism and derived explicit expressions for the scattering and absorption cross-sections, phase functions, and extinction coefficients of spherical particles.

Initially, Mie's theory received little attention in the scientific community due to the complexity of mathematical solutions. Moreover, the theoretical calculations were laborious, and the lack of computational tools in that era hindered its immediate practical applications. As a result, the full significance of Mie theory was not immediately recognized.

Mie's theory remained largely overlooked until the 1950s, when researchers started recognizing its potential significance for various fields, including atmospheric physics, astronomy, and materials science [62–64]. With the advent of computers and numerical methods, it became feasible to calculate Mie scattering for particles of different sizes and refractive indices, making it a powerful tool for experimental data interpretation and analysis.

As the use of Mie theory became more widespread, it was integrated with experimental techniques to characterize particles in various applications. For instance, it found application in particle sizing and characterization of aerosols, droplets, colloids, and biological particles [65–67].

Over time, modifications and extensions to Mie's theory were developed to account for different particle shapes, such as spheroids and cylinders, and to include additional factors like multiple scattering effects and particle ensembles in complex media.

Today, Mie theory continues to be a fundamental tool for understanding light scattering by particles. It remains as a crucial component of modern light scattering techniques used in diverse fields, including atmospheric science, remote sensing, environmental monitoring, and materials characterization. Its enduring relevance speaks to the profound impact of Gustav Mie's groundbreaking work on light scattering theory.

Specifically, Mie scattering is a theoretical model that describes light scattering by spherical particles, such as dust, water droplets, and biological cells [68–71]. While this theory is a powerful tool for understanding light scattering in many physical and

biological systems, there are several limitations to the model that should be considered [29,72]:

Size and shape: Mie scattering only applies to spherical particles with a uniform refractive index.

Size parameter: Mie scattering is most accurate for particles whose size is much larger than the wavelength of light being scattered. It may not be a good approximation for particles smaller than the wavelength of light or larger than several wavelengths.

Homogeneity: Mie scattering assumes that the medium in which the particles are suspended is homogeneous and isotropic. It may not accurately describe the scattering behavior if the medium is not homogeneous or if there are gradients in the refractive index or density.

Multiple scattering: Mie scattering assumes that the scattered light only undergoes a single scattering event. In reality, light can experience multiple scattering events, which can cause deviations from the Mie scattering predictions.

In Mie scattering theory, the scattered light is not uniformly distributed in all directions as opposed to Rayleigh scattering. Instead, the scattered light is concentrated in several directions, known as Mie resonances. These resonances are determined by the scattering particle's size and refractive index and the incident radiation's wavelength [60]. The theory has applications in a wide range of fields, including meteorology, remote sensing, and the design of optical devices.

This part gives the detailed derivation of Mie theory equations [49,50,60,73,74]to provide a complete understanding of the theory. Spherical coordinates of point P will be denoted as (r, θ, φ) with the usual meaning of the symbols. The vector OP which starts from the center of the sphere and goes through the radius and has the rectangular components (x, y, z) or $(r cos\varphi sin\theta, \ r sin\varphi sin\theta, \ r cos\theta)$ is denoted by **r**.

The scalar wave equation,

$$\Delta\psi + k^2 m^2 \psi = 0 \qquad (2.1)$$

where m is complex refractive index ($m = n_{part} + i\kappa$ and the imaginary part is ignored) of the particle, is separable in these coordinates and has elementary solutions of the following type:

$$\psi_{ln} = \left.\begin{matrix} cosl\varphi \\ sinl\varphi \end{matrix}\right\} P_n^l cos(\theta) z_n(mkr). \qquad (2.2)$$

Here, n and l are integers, $(n \geq l \geq 0)$, the first factor may be either a cosine or a sine; the second factor is an associated Legendre polynomial; the third factor may be spherical Bessel function defined by

$$z_n(\rho) = \sqrt{\frac{\pi}{2\rho}} Z_{n+1/2}(\rho) \tag{2.3}$$

in terms of ordinary Bessel functions. The general solution of the scalar wave equation is a linear combination of such elementary solutions.

By virtue of formulae $\nabla H = ikm^2 E$ and $\nabla E = -ikH$, the field vectors **E** and **H** in a homogeneous medium satisfy the vector wave equation.

$$\Delta \boldsymbol{A} + k^2 m^2 \boldsymbol{A} = 0. \tag{2.4}$$

Elementary solutions of this equation may be found from the following theorem. If ψ satisfies the scalar wave equation, the vectors $\boldsymbol{M}_\psi$ and $\boldsymbol{N}_\psi$ defined by

$$\boldsymbol{M}_\psi = \mathrm{curl}(\boldsymbol{r}\psi), \tag{2.5}$$

$$mk\boldsymbol{N}_\psi = \mathrm{curl}M_\psi, \tag{2.6}$$

satisfy the vector wave equation and are, moreover, related by

$$mk\boldsymbol{M}_\psi = \mathrm{curl}N_\psi. \tag{2.7}$$

A simple substitution shows that, if u and v are two solutions of the scalar wave equation and $\boldsymbol{M}_u$, $\boldsymbol{N}_u$, $\boldsymbol{M}_v$ and $\boldsymbol{N}_v$ are the derived vector fields, the Maxwell equations $\nabla H = ikm^2 E$ and $\nabla E = -ikH$ are satisfied by

$$\boldsymbol{E} = \boldsymbol{M}_v + i\boldsymbol{N}_u \tag{2.8}$$

$$\boldsymbol{H} = m(-\boldsymbol{M}_u + i\boldsymbol{N}_v) \tag{2.9}$$

The full components of $\boldsymbol{M}_\psi$ and $\boldsymbol{N}_\psi$ are

$$M_r = 0, \qquad mkN_r = \frac{\partial^2(r\psi)}{\partial r^2} + m^2 k^2 r\psi, \tag{2.10}$$

$$M_\theta = \frac{1}{r\sin(\theta)}\frac{\partial(r\psi)}{\partial\varphi}, \qquad mkN_\theta = \frac{1}{r}\frac{\partial^2(r\psi)}{\partial r\partial\theta}, \tag{2.11}$$

$$M_\varphi = -\frac{1}{r}\frac{\partial(r\psi)}{\partial\theta}, \qquad mkN_\varphi = \frac{1}{r\sin(\theta)}\frac{\partial^2(r\psi)}{\partial r\partial\varphi} \tag{2.12}$$

Starting with Maxwell's equations, an incident plane wave of electromagnetic radiation with a known wavelength and polarization interacts with a spherical particle. The incident wave (of amplitude 1) is described by Eqs. 2.13-2.14.

$$E = a_x e^{-ikz+iwt} \tag{2.13}$$

$$H = a_y e^{-ikz+iwt} \tag{2.14}$$

where a_x and a_y are unit vectors along the x- and y-axes, k is the propagation constant (= wave number) in vacuum and w is the frequency. Assume that the particle experiences an electric field due to the incident wave, which causes it to scatter radiation. A collection of outgoing spherical waves with various scattering angles and polarization components represents the scattered wave. By selecting u and v as the Eqs. 2.15-2.16, the same fields are expressed using the same format.

$$u = e^{iwt}\cos\varphi \sum_{n=1}^{\infty}(-i)^n \frac{2n+1}{n(n+1)}P_n^1(\cos\theta)j_n(kr) \tag{2.15}$$

$$v = e^{iwt}\sin\varphi \sum_{n=1}^{\infty}(-i)^n \frac{2n+1}{n(n+1)}P_n^1(\cos\theta)j_n(kr) \tag{2.16}$$

where j_n is the spherical Bessel function derived from the Bessel function of the first kind, $J_{n+1/2}$. The next step is applying the proper boundary conditions to the spherical particle's surface to maintain the continuity of the electric and magnetic fields. These conditions include that the electric and magnetic fields' tangential components are equal at the particle's surface.

On deriving the tangential field components, the following functions of the scattering angle, which are Legendre polynomials, appear:

$$\pi_n(\cos\theta) = \frac{1}{\sin\theta}P_n^1(\cos\theta) = \frac{dP_n(\cos\theta)}{d\cos\theta} \tag{2.17}$$

$$\tau_n(cos\theta) = \frac{d}{d\theta} P_n^1(cos\theta) = cos\theta . \pi_n(cos\theta) - sin^2\theta(d\pi_n(cos\theta))/dcos\theta \quad (2.18)$$

The boundary conditions of $\mathbf{n} \times (\mathbf{H_2} - \mathbf{H_1}) = 0$ and $\mathbf{n} \times (\mathbf{E_2} - \mathbf{E_1}) = 0$ are used to find the undetermined coefficients, where n is normal to the boundary surface. The field components E_θ and E_φ contain the expressions v and $\partial(ru)/n_{part}\partial r$. The components H_θ and H_φ contain mu and $\partial(rv)/\partial r$.

These four expressions must have equal values at either side of the boundary surface, $r = a$, where a is the radius of the sphere. The equations are simplified by defining a new set of functions that differs from spherical Bessel functions by an additional factor, z. The Ricatti-Bessel functions, Ψ, and ζ are defined by the half-integer-order Bessel function of the first kind as in Eq. 2.19 and Eq. 2.20, respectively, where

$$\Psi_n(z) = zj_n(z) = (\pi z/2)^{1/2} J_{n+1/2}(z) \quad (2.19)$$

$$\zeta_n(z) = zh_n^{(2)}(z) = (\pi z/2)^{1/2} H_{n+1/2}^{(2)}(z) = \Psi_n(z) + i\chi_n(z) \quad (2.20)$$

$$\chi_n(z) = -zn_n(z) = -(\pi z/2)^{1/2} N_{n+1/2}(z) \quad (2.21)$$

$H_{n+1/2}(z)$ is the half-integer-order Hankel function of the second kind and $X_n(z)$ is defined by half-integer-order Bessel function of second kind ($N_{n+1/2}(z)$) as presented in Eq. 2.21.

The argument, $x = ka = (2\pi an_{med})/\lambda$. Multiple components are formed from the scattered wave. Electric or magnetic dipole, electric or magnetic quadrupole, and other types of electromagnetic radiation scattering are all represented by distinct multipole terms.

$$[mu]: \quad \Psi_n(x) - a_n\zeta_n(x) = n_{part}c_n\Psi_n(n_{part}x) \quad (2.22)$$

$$\left[\frac{1}{n_p}\frac{\partial(ru)}{\partial r}\right]: \quad \Psi'_n(x) - a_n\zeta'_n(x) = c_n\Psi'_n(n_{part}x), \quad (2.23)$$

$$[v]: \quad \Psi_n(x) - b_n\zeta_n(x) = d_n\Psi_n(n_{part}x), \quad (2.24)$$

$$\left[\frac{\partial(rv)}{\partial r}\right]: \quad \Psi'_n(x) - b_n\zeta'_n(x) = n_{part}d_n\Psi'_n(n_{part}x). \quad (2.25)$$

By taking into account the interactions between the incident and scattered waves, scattering coefficients for the multipole expansion are calculated. This entails resolving

an equation system that fulfills the boundary conditions. On eliminating c_n from the first pair and d_n from the second pair of equations, the results are:

$$a_n = \frac{n_{med}\Psi'_n(n_{part}x)\Psi_n(x) - n_{part}\Psi_n(n_{part}x)\Psi'_n(x)}{n_{med}\Psi'_n(n_{part}x)\zeta_n(x) - n_{part}\Psi_n(n_{part}x)\zeta'_n(x)} \tag{2.26}$$

$$b_n = \frac{n_{part}\Psi'_n(n_{part}x)\Psi_n(x) - n_{med}\Psi_n(n_{part}x)\Psi'_n(x)}{n_{part}\Psi'_n(n_{part}x)\zeta_n(x) - n_{med}\Psi_n(n_{part}x)\zeta'_n(x)} \tag{2.27}$$

where n_{med} is the refractive index of the medium. For c_n and d_n, the Eq. 2.28, is found as common numerator with the same respective denominators.

$$\psi'_n(x)\zeta_n(x) - \psi_n(x)\zeta'_n(x) = i \tag{2.28}$$

The scattered wave

$$u = -\frac{i}{kr}e^{-ikr+iwt}\cos\varphi \sum_{n=1}^{\infty} a_n \frac{2n+1}{n(n+1)}P_n^1(\cos\theta) \tag{2.29}$$

$$v = -\frac{i}{kr}e^{-ikr+iwt}\sin\varphi \sum_{n=1}^{\infty} b_n \frac{2n+1}{n(n+1)}P_n^1(\cos\theta) \tag{2.30}$$

The resulting field components can be written at once in the form:

$$E_\theta = H_{\varphi=} -\frac{i}{kr}e^{-ikr+iwt}\cos\varphi S_2(\theta), \tag{2.31}$$

$$-E_\varphi = H_{\theta=} -\frac{i}{kr}e^{-ikr+iwt}\sin\varphi S_1(\theta), \tag{2.32}$$

where $S_1(\theta)$ and $S_2(\theta)$ are angular intensity functions as:

$$S_1(\theta) = \sum_{n=1}^{\infty} \frac{2n+1}{n(n+1)}\{a_n\pi_n(\cos\theta) + b_n\tau_n(\cos\theta)\}, \tag{2.33}$$

$$S_2(\theta) = \sum_{n=1}^{\infty} \frac{2n+1}{n(n+1)}\{b_n\pi_n(\cos\theta) + a_n\tau_n(\cos\theta)\}. \tag{2.34}$$

Differential scattering cross-sections are defined as given in Eq. 2.35 and Eq. 2.36.

$$\sigma'_{VV} = \frac{\lambda^2}{4\pi^2} |S_1(\theta)|^2 \tag{2.35}$$

$$\sigma'_{HH} = \frac{\lambda^2}{4\pi^2} |S_2(\theta)|^2 \tag{2.36}$$

where the subscription *VV* refers to vertically polarized incident light and vertically polarized scattered light with respect to incident scattering plane and as similar HH refers to horizontally polarized incident light and horizontally polarized scattered light. The other versions, VH and HV, have significantly smaller contributions that are generally ignored [61,73,74].

Scattering cross-sections are determined for various scattering processes, such as the total scattering cross-section, the absorption cross-section, and the scattering phase function. These numbers reveal the radiation's polarization, angular dispersion, and intensity. One can examine the scattering behavior for various particle sizes, refractive indices, and incident wave qualities after determining the scattering coefficients and cross sections. This analysis aids in understanding the optical characteristics and scattering patterns of the spherical particles [61,73,74].

2.3 Proposed System and Developments

Considering the consistent conditions of the current devices, such as huge device dimensions, high costs, maintenance requirements, and alignment issues, we need portable, low-cost, small setups due to rapidly increasing global microplastic problems. As stated in the introduction chapter, it is urgently needed to take precautions at the origin of those pollutants. Once it is possible to detect and classify those particles, it would be easier to define their source and define global measures to decrease the level of microplastic pollution.

In addition to micro size, with minor adjustments, it is possible to detect nano-size particles with the same setup. A thin lens to focus the light on a much smaller area and look for just a couple of particles instead of high concentrations and zoom the images taken at the laboratory would open another window to research on nano plastics.

Furthermore, once the appropriate solvents, concentrations, and incident light are provided, it would be possible to investigate different types of particles. This point will be stated again as future prospects part of this thesis.

In Figure 2.2, the illustration of the experimental setup is presented. Directing a laser beam onto samples in a cuvette through an iris and neutral density filter is the part before scattering occurs. When light hits the particles in the cuvette, it scatters, and the pattern falls onto the screen behind. Having particles at different sizes, refractive indices, and concentrations and using different wavelength of incident lights results in different scattering patterns. Thus, by a cost-effective setup, unique scattering patterns are acquired.

Figure 2.2 Illustration of the experimental setup, (a) light source, (b) iris, (c) neutral density filter, (d) cuvette holder and cuvette, and (e) graded white screen, (inset) azimuthal and scattering angles.

Once the raw images are collected from the setup (Figure 2.3(a)), we crop them and obtain the upper right quartile as in Figure 2.3(b). This is possible because of spherical particles that scatter light symmetrically, so we work on this quarter only to decrease

computational cost. Next, we convert the image into grayscale (Figure 2.3(c)). Comparison of red, green, and blue images is possible when we analyze them in the gray version. Then, we draw azimuthal lines from the center through the outer rings to get scattering information. Again, symmetry gives each line the same pixel values on it. To decrease noise and error, we take the average values on that azimuthal line (Figure 2.3(d)), and the scattering information is ready to plot as given in Figure 2.3(e).
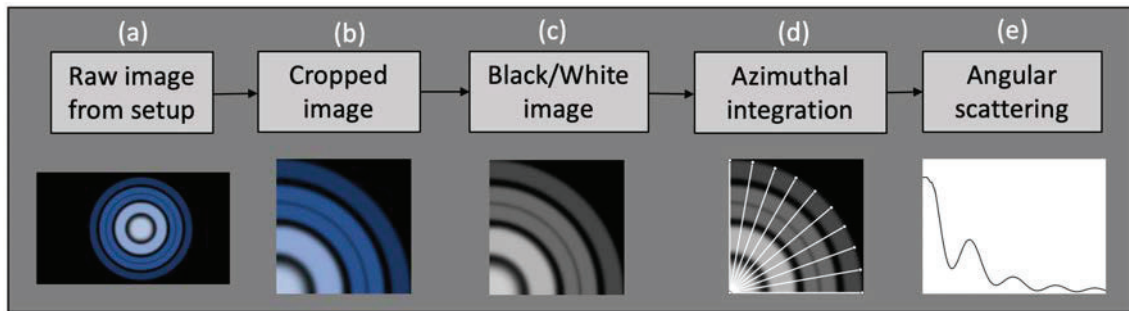
Figure 2.3 Representation of image processing flow from the raw image to the scattering pattern.

The peaks on that scattering line represent bright interference rings, and the gaps are destructive combinations. Having different samples mean having different patterns and different scattering lines. After all those steps, different sets of peak angles are aimed to use as random forest algorithm inputs.

Chapter 3

Experimental Work

3.1 Sample Preparation

Investigating the impact of material type (particle's refractive index) and particle size is possible using commercially available microparticles made of two different materials, melamine (Me) and polystyrene (PS), at diameters of 8 μm and 10 μm. In order to examine the relationship between particle number and scattering behavior, we also generated samples at various concentrations.

Commercially available 8 μm $\pm$ 100 nm-sized melamine resin (Me8) (95523-Sigma Aldrich), 8 μm $\pm$ 97 nm-sized Polystyrene (PS8) (84192-Sigma Aldrich) and 10 μm $\pm$ 110 nm-sized Polystyrene (PS10) (72986-Sigma Aldrich) microspheres, were used in the experiments to test the match between the predictions of Mie theory that we calculated numerically and the experimental results. Microscope images of Me and PS spheres are given in Figure 3.1.
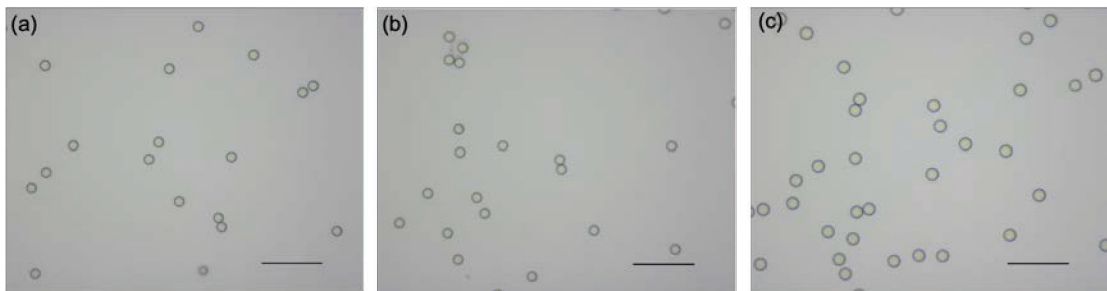
Figure 3.1 40x-zoomed microscope images of (a) Me8, (b) PS8, and (c) PS10 particles. Scale bar: 50 μm.

Samples were prepared at the concentrations from 0.05 fM up to 3.00 fM by adding them into ultra-pure water using a micropipette and kept in vials, Figure 3.2. The samples were shaken using a vortex before the experiments to make the solution much more homogeneous and by hand just before the measurements one more time.
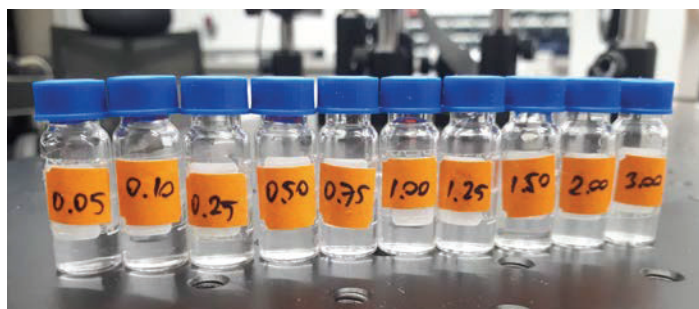
Figure 3.2 Samples prepared at different concentrations.

In our experiments, the safe time limit was about 5 minutes. The sinking of the particles deeper in the cuvette and around 5% decrease in scattering intensity was observed after 5 minutes. Our measurement time for each sample was much shorter than this limit. In addition, 0.05 - 3.00 fM range corresponds to $3 \times 10^4 - 180 \times 10^4$ particles/mL, higher than the values studied in the literature. However, the sizes of the particles reported in the literature are about 10-100 times bigger, significantly increasing the scattering cross-section. Considering this size difference, we believe that it is reasonable to have 0.05 fM - 3.00 fM concentration range in our experiments for the particle sizes we are interested in [75].

There is an uncertainty in the literature regarding the refractive index of Melamine particles [76–78]. Thus, we studied the range given in the literature, 1.530-1.922, for the red wavelength range. The most satisfying match with the Mie theory and experiments was obtained as 1.79 at 656.3 nm. We used refractive indices of 1.89 and 1.96 for 514.9 nm and 403.8 nm, respectively.

3.2 Experimental Setup

For the measurements, at room temperature (22 ºC), the laser power was kept between 150 - 170 μW for collimated blue, green, and red lasers emitting light at 403.8 nm, 514.9 nm, and 656.3 nm, respectively (CPS405, CPS520, and CPS650F-THORLABS). The beam was directed through an iris to squeeze the beam radius. Just after the iris, a neutral density filter was used to adjust the laser power to the same level during the experiments. A cuvette holder was 3D printed to keep the cuvette in the optimum orientation. Finally, a graded white screen was placed to have the scattering pattern, as presented in Figure 3.3.

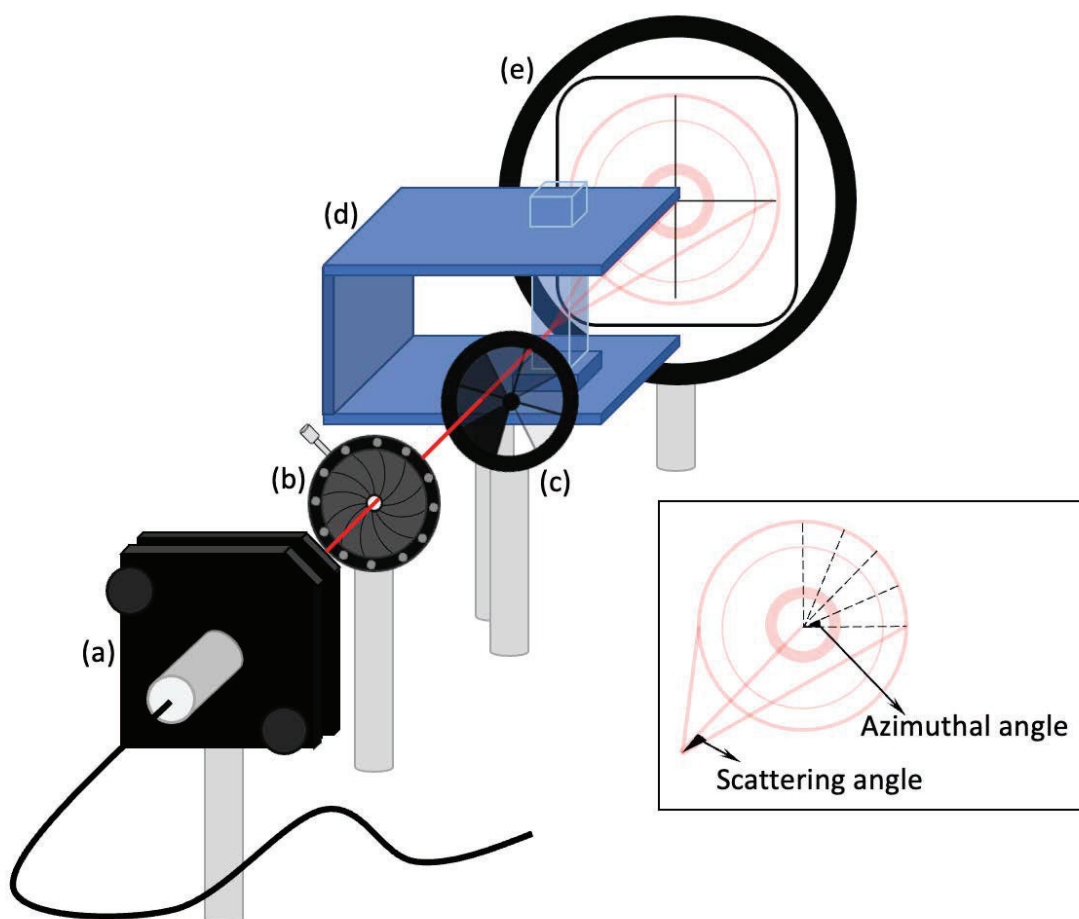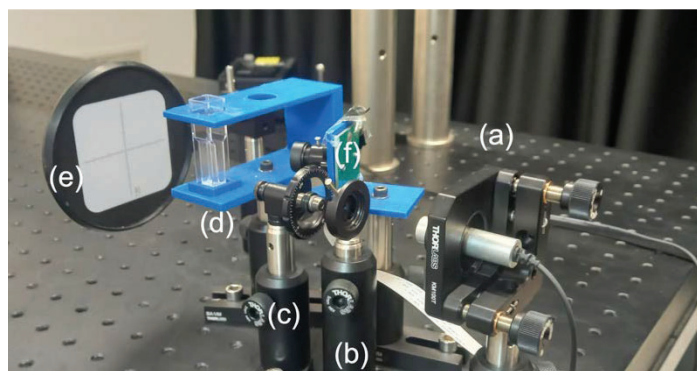**Figure 3.3 Experimental setup, (a) light source, (b) iris, (c) neutral density filter, (d) cuvette holder and cuvette, (e) graded white screen, and (f) camera module.**

Subsequently, each sample was placed into cuvettes, and the scattering patterns of the laser light at different wavelengths from these particles fell on a screen set 6.5 cm apart from the cuvette. 200 images of these scattering patterns were taken in a dark environment by a CMOS camera (Raspberry Pi Focus Adjustable Camera Module- 2592x1944 pixels), -100 ms shutter speed and 20 ms exposure time- controlled by Raspberry Pi 4 - 4GB RAM. In total, 1800 images are recorded for processing.

3.3 Image Processing

Recorded images required following image processing steps to obtain some digital data to be used in machine learning. For each sample, 200 images were taken, and processing individually was not possible due to the high level of noise.
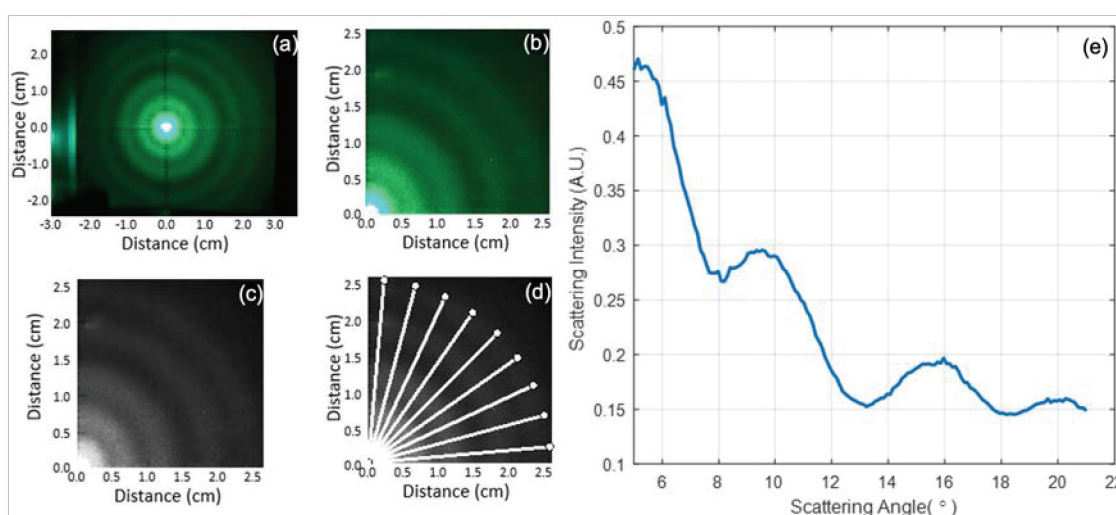
Figure 3.4 (a) Raw scattering image of Me8 particles excited by a green laser, (b) cropped image, (c) gray-scale image, (d) data lines on scattering image, (e) average scattering behavior of 86 lines (5°:1°:90°) on 1.50 fM 8 μm Me particles.

The images of the scattering patterns (Figure 3.4(a)) were analyzed numerically. To minimize noise, the average of 200 images was calculated for each sample's scattering pattern. Next, as illustrated in Figure 3.4(b-c), all the images were cropped and converted to grayscale. To decrease the computational cost, 86 lines were defined with 1º azimuthal angle increments between 5º and 90º starting from the center towards the outer regions on the upper-right quartile of the images as given in Figure 3.4(d), (Figure 3.4(d), presents only 10º azimuthal increment for better visualization). As the next step, the average pixel data on all those 81 lines was taken to decrease the noise level on measurements. Finally, azimuthal angular scattering intensity was obtained, as presented in Figure 3.4(e). However, it was still noisy to identify peak angles. Therefore 2nd-degree polynomial was fitted to the experimental data around each peak because fitting a polynomial with an exact high degree, i.e., 25th, was not an appropriate match for every scattering data point. We assumed that fitting a second-degree polynomial would provide consistent methodology during the analysis. Therefore, using an angle range from the left and right side of each peak, we fit a second-degree polynomial and used the angle of the peak point as experimental peak angles.

3.4 Random Forest Algorithm

Random Forest is a popular machine-learning algorithm for classification and regression tasks. It is an ensemble learning method that creates a set of decision trees and combines their predictions to make a final prediction [79–81].
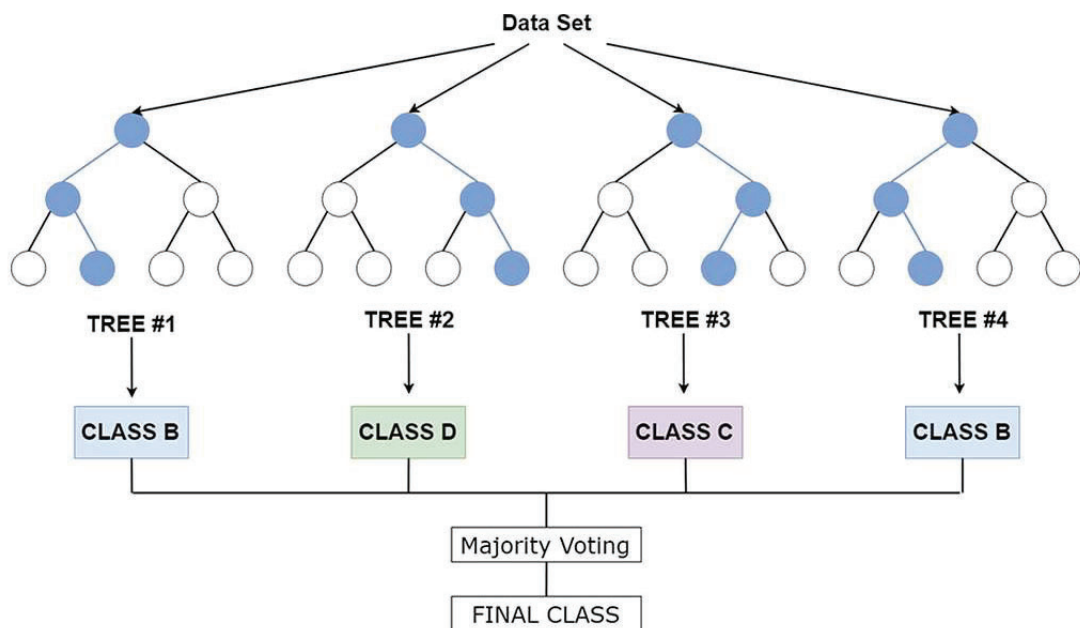
Figure 3.5 Structure of random forest algorithm [82].

The algorithm works by randomly selecting a subset of the data and a subset of the features for each tree in the forest. Then, a decision tree is built using these subsets of data and features. The process is repeated multiple times, resulting in a forest of decision trees, as presented in Figure 3.5.When predicting a new data point, each tree in the forest independently makes a prediction, and the final prediction is made by taking the majority vote of all the trees in the forest.

Random Forest has several advantages over a single decision tree. It is less prone to overfitting, as the individual trees in the forest are trained on different subsets of the data and features. It can handle high-dimensional data and is relatively easy to use, as it requires a few hyperparameters to be tuned.

Given the inherent numerous scatterings of the spheres in liquid, the random forest algorithm offers the opportunity to categorize the measured scattering data, which would not be a simple operation to manage theoretically. Random forest was utilized in this investigation because of its straightforward design and repeatable outcomes. The correspondence between experimental findings and numerical solutions, explained in detail in the following chapters, provided the opportunity to use numerical solutions for further analysis. This match made it possible to apply random forest easily for data preparation. This numerical solution methodology produced the data set, including the incidence wavelength, particle size, material type, and bright ring angles used to run the algorithm. A test set of data was created from 20% of all measurements. The remaining part was used to train the random forest algorithm.

The inputs for classifying material types and particle sizes were wavelength of incident light and bright ring angles. The concentration and scattering intensities were not required for this stage because it was discovered during the image analysis that the peaks were at the same angle for a specific material type and size. However, we are aware that as sphere concentration in samples grew, the total scattering intensity also had to rise.

Overall, Random Forest is a robust and widely used algorithm in machine learning that can be used for various tasks, such as classification, regression, and feature selection.

Chapter 4

Effects of Concentration, Particle Size, Material, and Wavelength of Incident Light

There are parameters affecting scattering during the investigation of scatterers. The concentration of particles, particle size, refractive index, material that particles are made of, and wavelength of incident light. In this chapter, the effects of those parameters will be investigated, and their relevance to this study will be discussed. Experimental and theoretical results will be given. For theoretical results, equations were embedded in a MATLAB code, which is given in Appendix A.

4.1 Effect of the Sample Concentration on Scattering

The intensity and pattern of Mie scattering can be affected by the concentration of the scattering particles. At low concentrations, Mie scattering is typically linearly proportional to the concentration of the scattering particles. This means that if the concentration of the scattering particles is doubled, the intensity of the scattered light will also double. However, the relationship between Mie scattering and particle concentration at high concentrations becomes more complex.

At high concentrations, the particles can interact with each other, leading to a phenomenon known as multiple scattering. Multiple scattering can cause the scattered light to be redirected and interfered with, resulting in a more complex scattering pattern. In extreme cases, the numerous scatterings can lead to a phenomenon known as optical turbidity, where the scattered light is so intense that it can obscure the light source and reduce the visibility of the scattering particles.
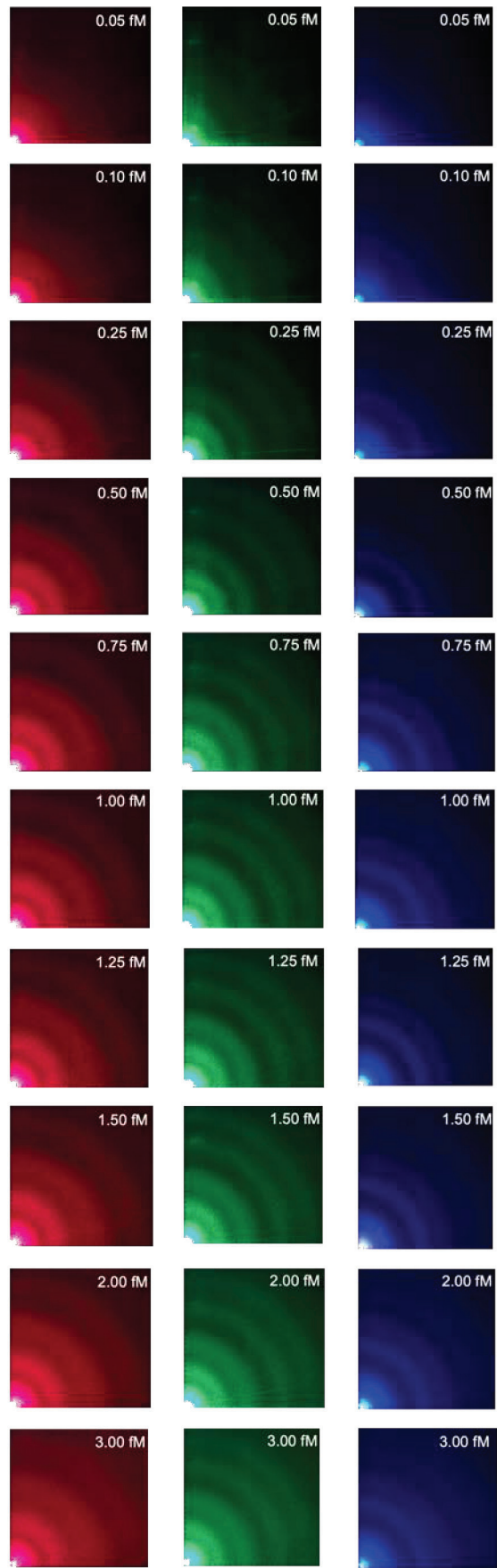
Figure 4.1 Scattering images of Me8 particles by red, green, and blue lasers with increasing concentration.

In Figure 4.1, it is presented that the scattered light intensity has a direct relation with number of the particles in samples which is called concentration. The effects of concentration on Mie scattering can range from a linear increase in scattering intensity at low concentrations to complex multiple scattering and optical turbidity at high concentrations.

It was explained in Chapter 1 that forward scattering is dominant in Mie scattering. Considering the equations in Chapter 2, when the number of particles increases, the scattered light at close to zero angles joins the zero-degree scattering, and forward scattering increases the intensity. Therefore, increasing the concentration is expected to result in brighter and wider centers on images. In Figure 4.2, scattering of (a, b, c) Me8, (d, e, f) PS8, and (g, h, i) PS10 particles are presented. As expected, scattering intensity gets higher with increasing concentration from 0.05 fM to 3.00 fM. In this figure, (a, d, g), (b, e, h), and (c, f, i) represents red, green, and blue light, respectively.
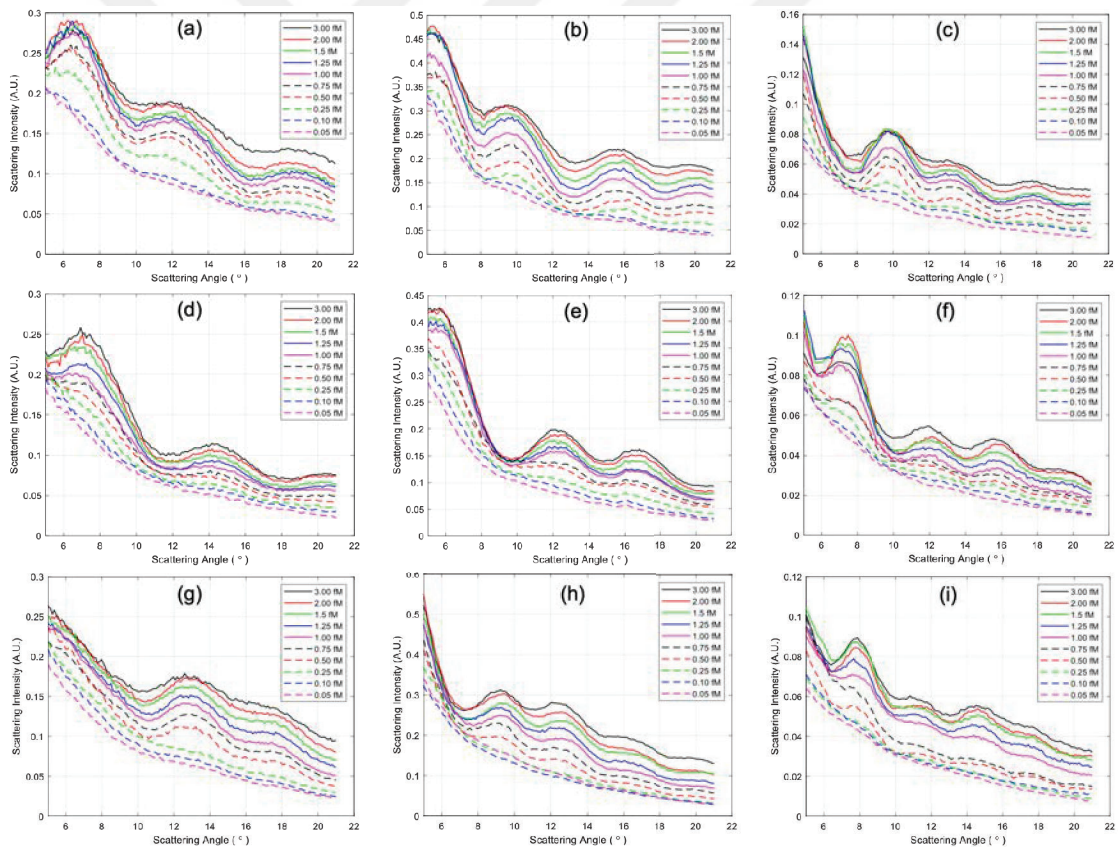
Figure 4.2 Scattering intensity vs. concentration change for Me8 (a, b, c), PS8 (d, e, f), and PS10 (g, h, i) materials by red (a, d, g), green (b, e, h), and blue (c, f, i) lasers.

In addition to the concentration, the settlement of the particles is also important. As discussed in previous chapters, particles are shaken by vortex before experiments and by hand just before the measurements. However, due to gravity, particles move towards the

bottom of the cuvettes during the photoshoot. If those particles go down fast, there will be less than the targeted concentration, leading to less scattering intensity. Less scattering intensity may have two meanings. First, particles move down too fast, and we lose information; second, the sample concentration is less than targeted. To investigate this issue, instead of 200 images per sample, 800 images were taken consecutively. Grouping them as 100-image packages and plotting their scattering information on the same graph with the closest higher and lower concentration samples would give us information about the reliability of our measurement. In Figure 4.3, gray-scale images belonging to an average of 100 consecutive images of the same sample. As is not possible to conclude from raw images directly, so we performed image processing steps and obtained scattering lines for those image packages.
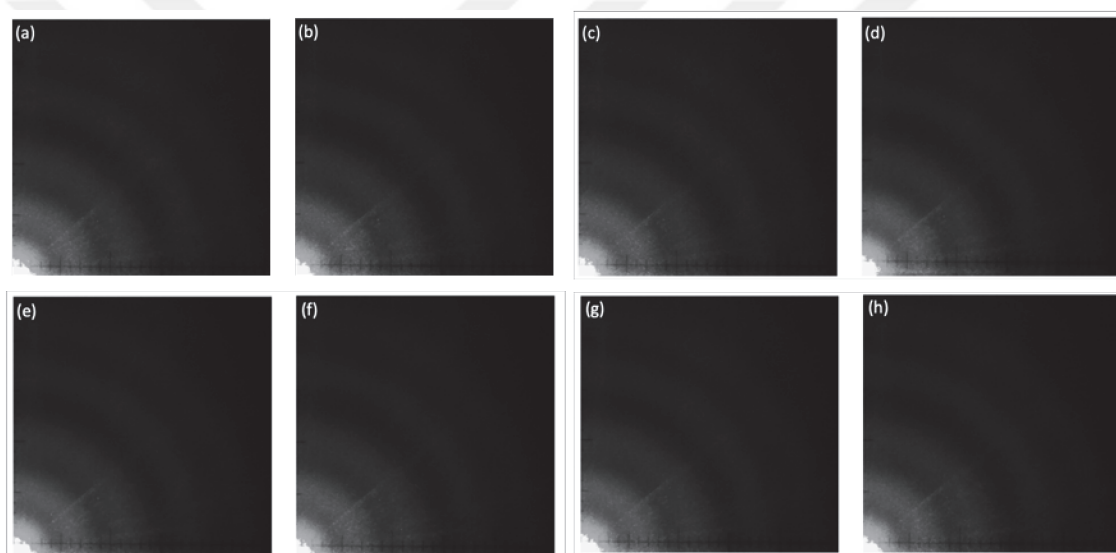
Figure 4.3 Scattering patterns for 2.00 fM PS8 particles for consecutive 100 images. (a) 1-100th, (b) 101-200th, (c) 201-300th, (d) 301-400th, (e) 401-500th, (f) 501-600th, (g) 601-700th, and (h) 701-800th.
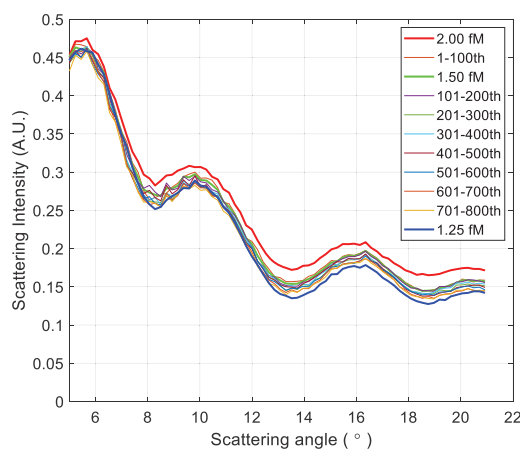
Figure 4.4 Scattering intensity change by time for PS8 particles excited by a green laser.

As given in Figure 4.4, even the last package of 100-image (701-800), meaning that the lowest scattering intensity among the groups has higher scattering intensity than the closest lower one, 1.25 fM. Therefore, settlement is not an issue in our measurements.

Scattering intensity is important while determining the concentration of particles. The area under scattering lines gives information about how much light is scattered, which is directly related to the concentration. We calculated the areas under scattering lines for three different measurements and plotted that data. Then, fitting a curve as a calibration curve provided information about the amount of scattered light scattered vs concentration. By using this curve, it is possible to obtain concentration information of a sample by using the amount of scattered light. After that point, it is just an image processing step to calculate the value for an unknown concentration to define its value.
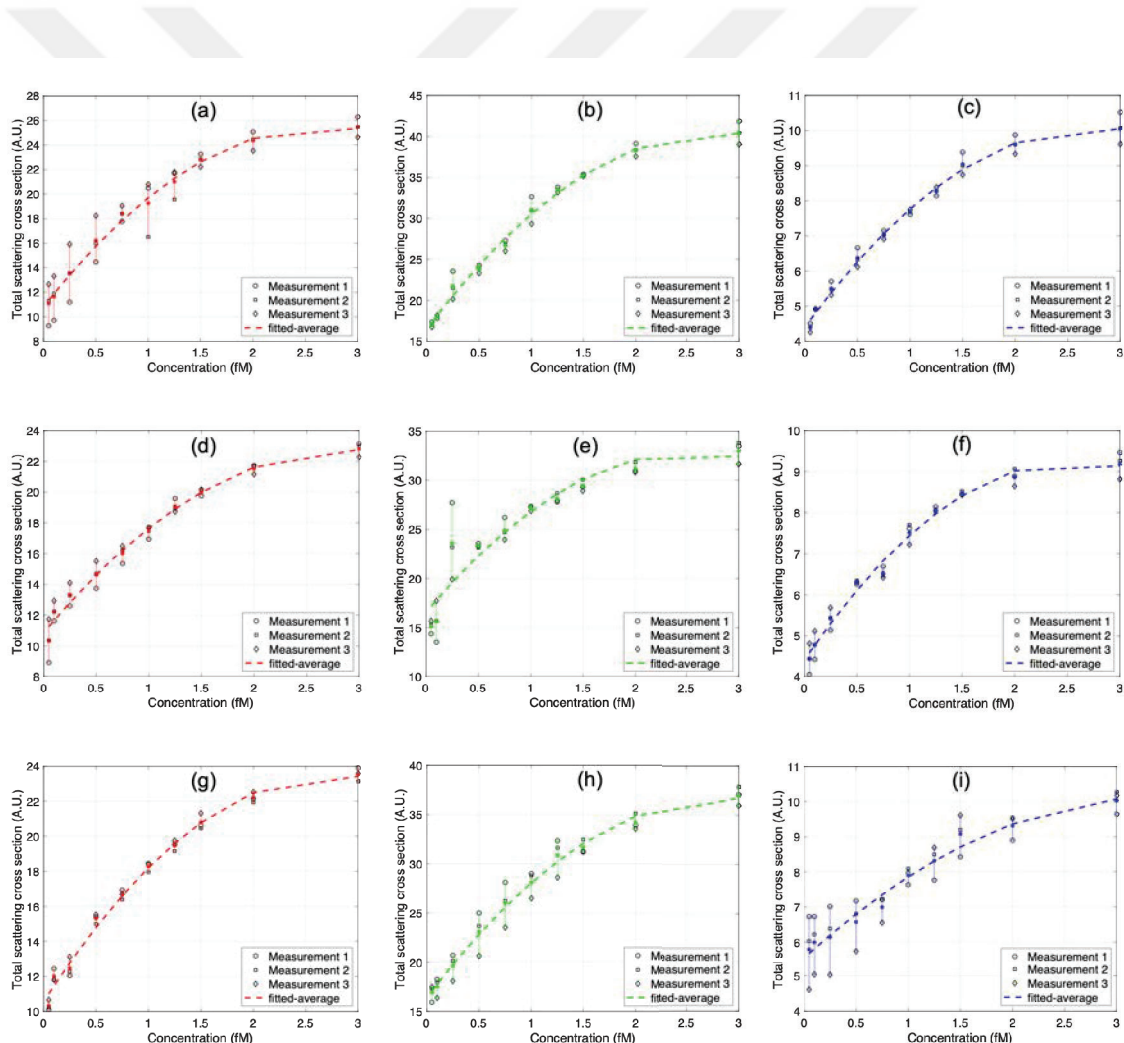
Figure 4.5 Total scattering intensity vs concentration change for Me8 (a, b, c), PS8 (d, e, f) and PS10 (g, h, i) materials by red, green, and blue lasers.

As presented in Figure 4.5, there are different calibration curves for different particle sizes, wavelength of incident light, and refractive index. (a, b, c) represents Me8,

(d, e, f) represents PS8 and (g, h, i) represents PS10 particles. Three columns in figure present red, green, and blue light, respectively. It is known that scattering is dependent on all those parameters. If there are enough different particles and lasers, a general equation can be generated depending on particle size, refractive index, concentration, power, and wavelength of incident light.

To sum up, after the experiments, we observed that, as expected, forward scattering gets dominant with increasing concentration. In addition, the same sample scatters at the same peak angles, interference rings, and this provides an opportunity to use those interference ring angles specifically for that material identification. In our concentration range, because the lines go saturation, it shows that we already reached the limit of our setup to determine the concentration of the samples.

4.2 Effect of Particle Size on Scattering

In Mie scattering, the scattered light depends strongly on the particle size and the particle's refractive index. As presented in Figure 4.6, for bigger particles, peaks of scattered light moves through the zero angle and make the forward scattering dominant. Although figure represents only first four peak angles, it can be estimated that for bigger particles, there are more peak points than smaller particles.
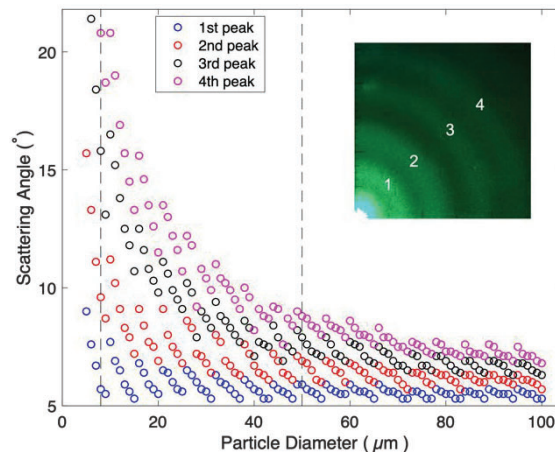
Figure 4.6 Angular distribution of the first four scattering intensity peaks to the particle size as calculated using Mie theory. The particle size was varied between 5-100 μm in water and 514.9 nm incident light beam in MATLAB, (inset) experimental image showing peaks (greater than 5°) for 8 μm.

The size of the particle determines the angle and intensity of the scattered light. In general, smaller particles scatter light more in the forward direction, while larger particles

scatter light more in the backward direction. This is because larger particles diffract light more, causing it to scatter in multiple directions.
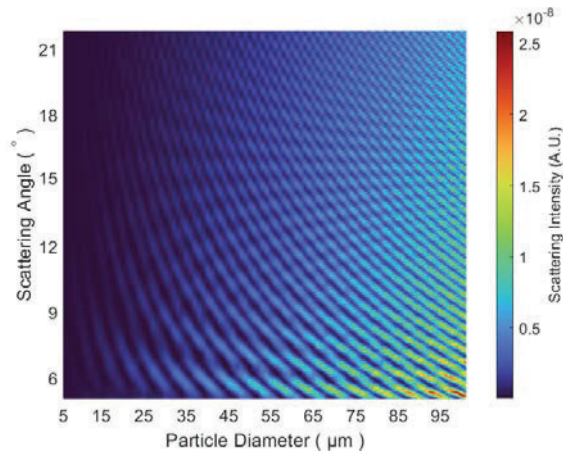
Figure 4.7 Total scattering intensity vs. particle size change for Me8 particles by green laser.

In the same medium (water) and using the same wavelength of the incident light, the effect of particle size was investigated to study how angular scattering changes based on numerical calculations. In Figure 4.7, the peaks of the scattering angles as a function of particle size were presented for the green light (at a wavelength of 514.9 nm) and water (n=1.3344). The particle diameter increases from 5 to 100 μm with a step size of 1 μm. For a given wavelength of light, there is a characteristic size of particle that scatters the most light in the forward direction, called the Mie scattering peak. The Mie scattering peak is shifted to smaller angles for shorter wavelengths of light.

In laboratory experiments, to be able to monitor the effect of particle size, PS8 and PS10 particles were used. 8 and 10 μm size of those particles provided information about particle size parameters when other parameters, i.e., wavelength of incident light, particle refractive index, and concentration, were constant. As expected, forward scattering became dominant when the size of Polystyrene particles increased. More peaks at the same range of scattering angle (5- 21 degrees) present that the scattered light at small angles got closer even combined with zero-degree scattering. Thus, as given in Figure 4.8, 10 μm-size PS particles have a brighter spot at the center and a brighter interference ring at the same range of images.
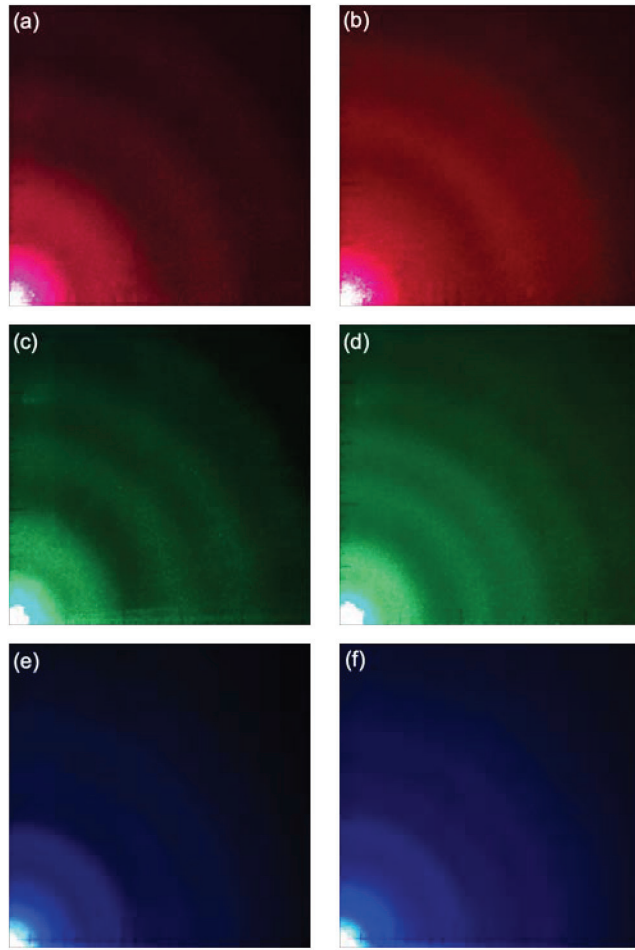
Figure 4.8 Scattering patterns of PS8 (a, c, e) and PS10 (b, d, f) particles at 1.50 fM concentration to monitor particle size effect by 656.3 nm, 514.9 nm, and 403.8 nm lasers.

In summary, the particle size significantly affects Mie scattering, with smaller particles scattering more light in the forward direction. In comparison, larger particles scatter more light in the backward direction. The Mie scattering peak is shifted to smaller sizes for shorter wavelengths of light.

4.3 Effect of Particle Refractive Index on Scattering

The refractive index of particles affects the scattering pattern because it determines the phase shift of the scattered wave relative to the incident wave. This phase shift is caused by the change in the speed of light as it passes from one medium (air) to another (the particle).

In Figure 4.9, the relation between refractive index of the particle and scattered light intensity is investigated. In (a, c, e), the transition of scattered light intensity and (b, d, e) the peak angles are presented. As expected, while red laser (a, b) has wide but low number

of peaks, the blue (e, f) has many but narrower peaks. Also, increasing the refractive index of the particle creates more peaks but decreases the intensity of each peak of scattered light.
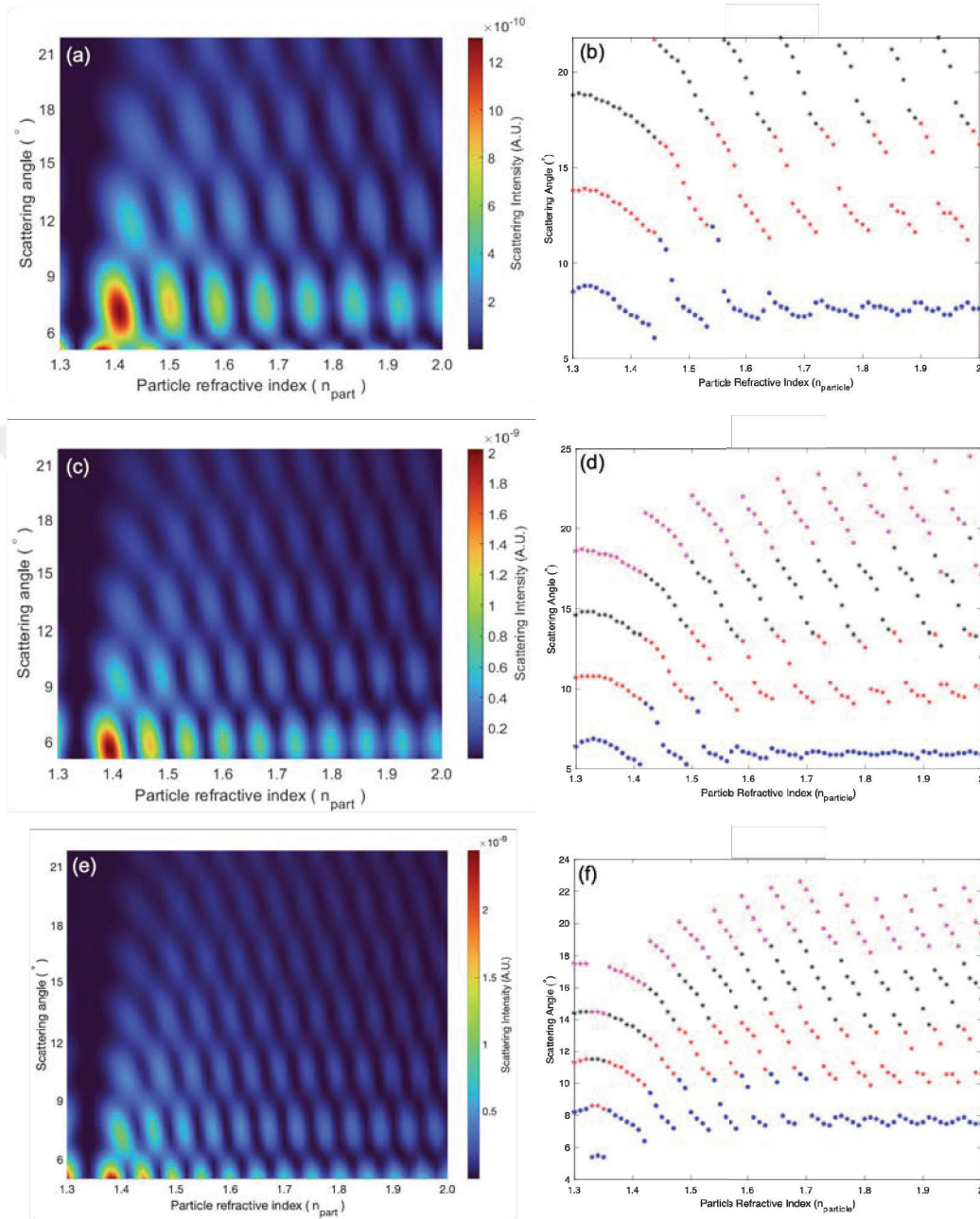
Figure 4.9 Scattering intensities vs. particle refractive index for red, green, and blue lasers (a, c, e), locations of first four peak angles vs. particle refractive index for red, green, and blue lasers (b, d, f).

In the laboratory, Me8 and PS8 particles were used to investigate the effect of particle refractive index. This is one of the key points of this study -it is worth repeating-there is a lack of study in terms of the same size and shape but material of particle in the literature. Theoretically, if a particle has a higher refractive index value than those with a lower refractive index, it scatters the light with wider angles. Therefore, fewer bright

interference rings are observed at the same distance from the center of an image. As presented in Figure 4.10, the left column (Me8 with lower refractive index) has more rings than the right one (PS8 with higher refractive index). It should not be forgotten to compare the refractive indices at proper wavelengths due to dispersion.
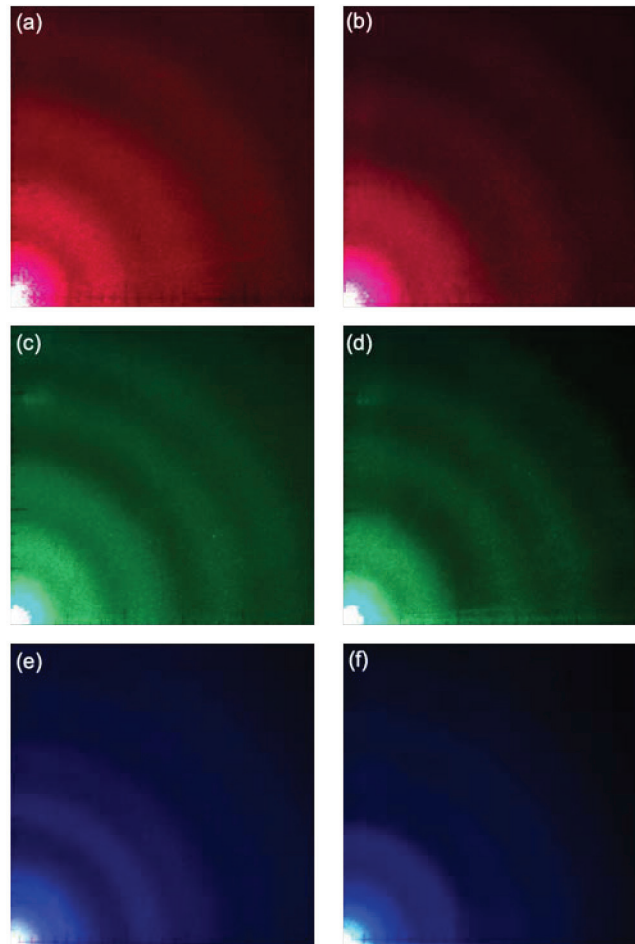
Figure 4.10 Scattering patterns of Me8 (a, c, e) and PS8 (b, d, f) particles at 1.50 fM concentration to monitor refractive index effect by 656.3 nm, 514.9 nm, and 403.8 nm lasers.

In summary, the refractive index of particles plays a crucial role in Mie scattering by influencing the scattering angle and polarization of the scattered light.

4.4 Effect of Incident Light's Wavelength on Scattering

The scattered radiation depends on the particles' size, shape, and refractive index, as well as the incident wavelength of the radiation. The size parameter, defined as the ratio of the particle radius to the wavelength of incident light, determines the scattering

behavior of Mie scattering. As the size parameter increases, the scattering pattern changes from forward to backward scattering.

Generally, the scattering strongly depends on the wavelength of incident light for small particles (size parameter << 1). When the size of the spherical particle is comparable to the wavelength of the incident radiation, the scattered light undergoes constructive and destructive interference, leading to complex scattering patterns. This phenomenon is known as resonance scattering. The resonance wavelength, at which the scattering is the strongest, depends on the size and refractive index of the particle.
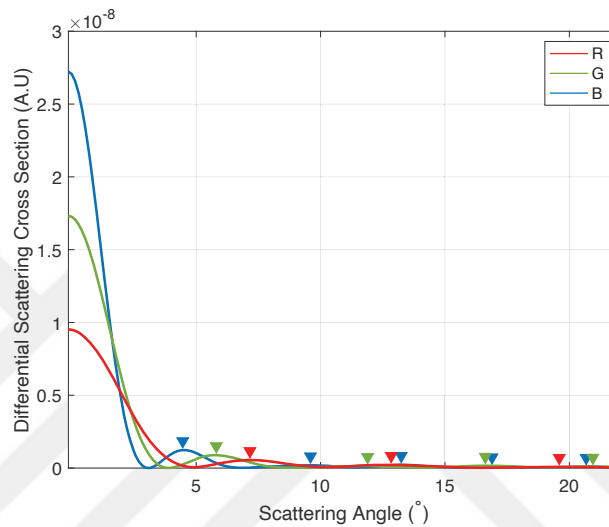
Figure 4.11 Calculated angular distribution of the scattering cross-section of 8 μm-sized particles in water for three different wavelength of incident lights. The triangles represent the locations of the scattering peaks.

As the wavelength of incident light increases, the scattering becomes less sensitive to the size of the particle, and the scattering pattern becomes more uniform as presented in Figure 4.11. This is because the effect of resonance scattering diminishes as the particle size becomes small compared to the wavelength of the incident radiation. In this case, the scattering pattern becomes more similar to Rayleigh scattering, which occurs when the size of the particle is much smaller than the wavelength of the incident radiation.

It is the starting point of this study in the laboratory. We were expecting that different incident lights (lasers) needed to provide different scattering patterns, and it had to be observable. In addition, different sizes of the same particle, and different particles at the same size were aimed to result in different images. All those expectations occurred successfully. We could observe those different patterns using a cost-effective setup of a few hundred euros. In addition, three different sample sets and measurements at different times provided consistent results.
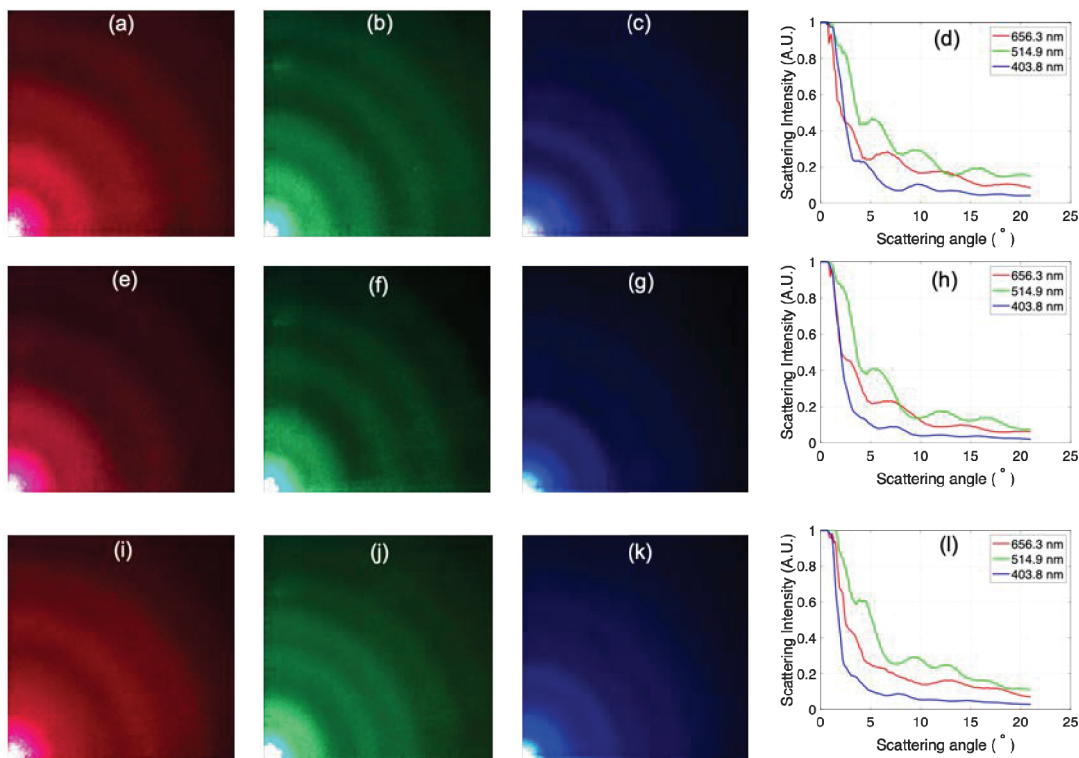
Figure 4.12 Scattering patterns of Me8 (a,b,c), PS8 (e,f,g), and PS10 (i,j,k) particles at 1.50 fM concentration and their scattering data to monitor wavelength of incident light effect by 656.3 nm (d), 514.9 nm (h), and 403.8 nm (l) lasers.

In Figure 4.12, it can be seen that for Me8 particles (a, b, c) we see a smaller number of peaks than PS8 particles (e, f, g) where Me8 has higher refractive index than PS8. Also, PS10 (i, j, k) have narrower peaks and higher intensities than PS8 (e, f, g) as a result of bigger size. All those patterns show the consistency between theoretical expectations and experimental results.

In summary, the wavelength of incident light affects Mie scattering by determining the resonance wavelength, which is the wavelength at which scattering is the strongest. As the wavelength increases, the scattering becomes less sensitive to the size of the particle, and the scattering pattern becomes more uniform.

4.5 Analysis of Mixture of Particles in One Sample

As a further step, melamine and polystyrene particles were mixed at known concentrations to investigate and characterize multiparticle samples. This provides a closer approach to real-life cases.

Me8-PS8, Me8-PS10, and PS8-PS10 pairs were mixed at a 1:1 ratio for 0.50 fM, 1.00 fM, and 1.50 fM concentrations. In total, nine combinations for each wavelength of

incident light were investigated for each pair. In addition, UPW measurements were done to observe the light scattering in a particle-free environment. The aim was to reveal the relationship between the individual scattering of two samples and their combination.

In this part of the study, we experienced several challenges. First, some of the particles stuck to each other and created a bigger form which caused a zero-angle dominant scattering and less intensity at wider angles. This was an expected result because, as explained in part 4.2, forward scattering gets dominant for bigger particles, and a lower light intensity is observed at wider angles compared to the smaller particles' scattering, as presented in Figure 4.13.
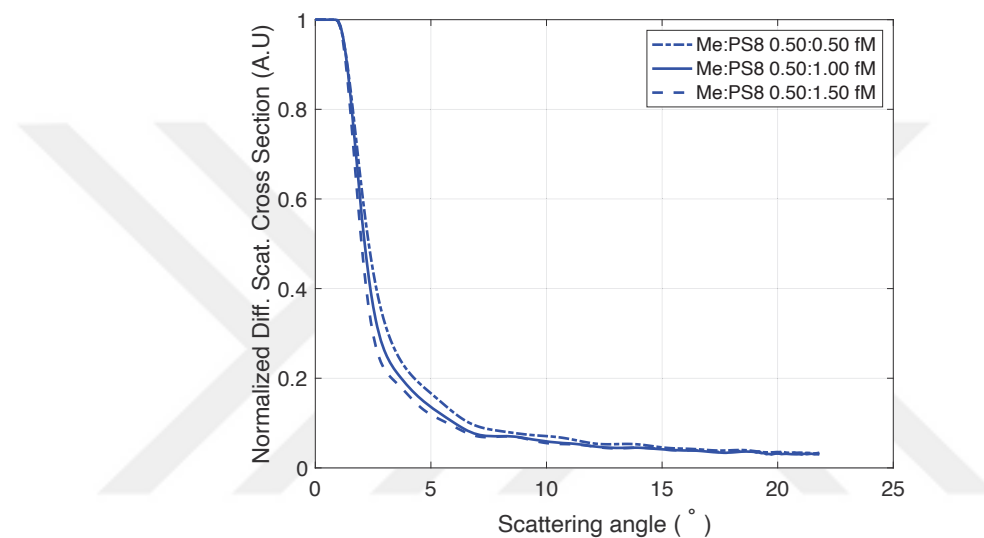
Figure 4.13 Scattering of Me8 and PS8 particles at 1:1 ratio for 0.50 fM Me8 with 0.50 fM PS8, 1.00 fM PS8, and 1.50 fM PS8 concentrations by blue light.

Another problem was revealing the relation between individual scatterings and the combination. Even though there were only two different types of particles regarding the size or material type, the scattering of the mixture could not be related to the individual scattering information as given in Figure 4.14, a mixture of two particles (a) with different sizes, (b) same size but composed of different materials.
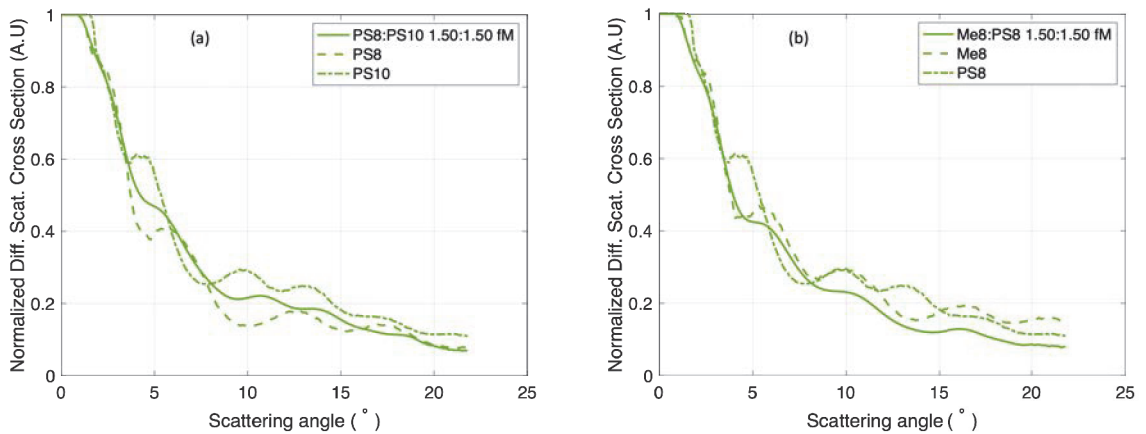
Figure 4.14 Scattering of (a) PS8 and PS10 particles at 1:1 ratio for 1.50 fM PS8 with 1.50 fM PS10, (b) Me8 and PS8 particles at 1:1 ratio for 1.50 fM Me8 with 1.50 fM PS8 by green light.

This behavior may occur because of the size distribution, homogeneity, or multiple scattering. Here, as we assume, if we have particle size distribution at a broader range, more than two different size values, instead of bright peak angles, we will observe a cloudy pattern with scattered light but no peaks.

At this point, compared to the particle-free, UPW scattering patterns, we observe a clear difference where we can talk about the existence of the microplastics in a sample. However, we cannot characterize this with a low-cost setup, as presented in Figure 4.15. There may be need for more detectors, lenses to change focus etc.
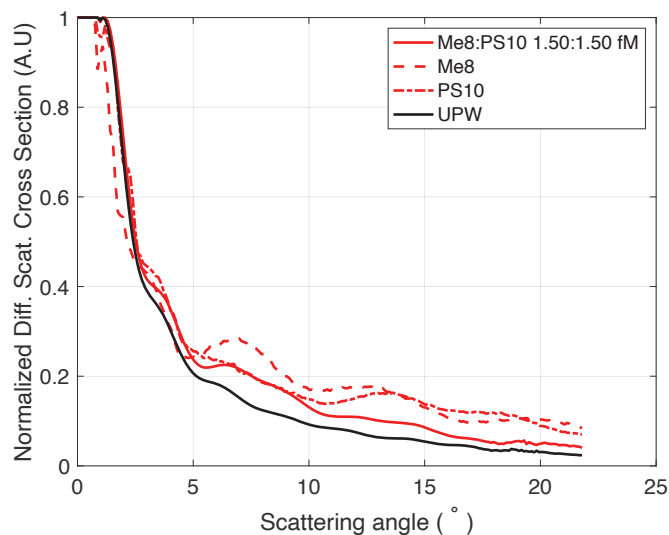
Figure 4.15 Scattering of Me8 and PS10 particles mixture at 1:1 ratio for 1.50 fM Me8 with 1.50 fM PS10 and ultra-pure water (UPW) by red light.

Chapter 5

Machine Learning Integration

Previous chapters showed that the equations to calculate scattering is difficult and complex for hand calculations. Thus, they were embedded in numerical solvers. However, for rapid analysis and ease of use, integration of machine learning into the setup would dramatically increase the performance of this study.

Using the equations, peak angles (bright interference ring angles) are obtained from the theory. In real-life applications, instead of the inputs we use to get those peak angles, we have the output, the pattern of scattering. So, reverse engineering is needed for the theoretical calculations. In this study, we aimed to show the match between theory and experimental results limited by two materials, Me and PS. Furthermore, only 8 and 10 μm-sized particles were used to prepare samples for investigation. There will be much more options in real-life applications.

In Figure 5.1, it is presented that the match between theory and experimental results is satisfying—slight differences between those results provided the opportunity to create a dataset for further developments.
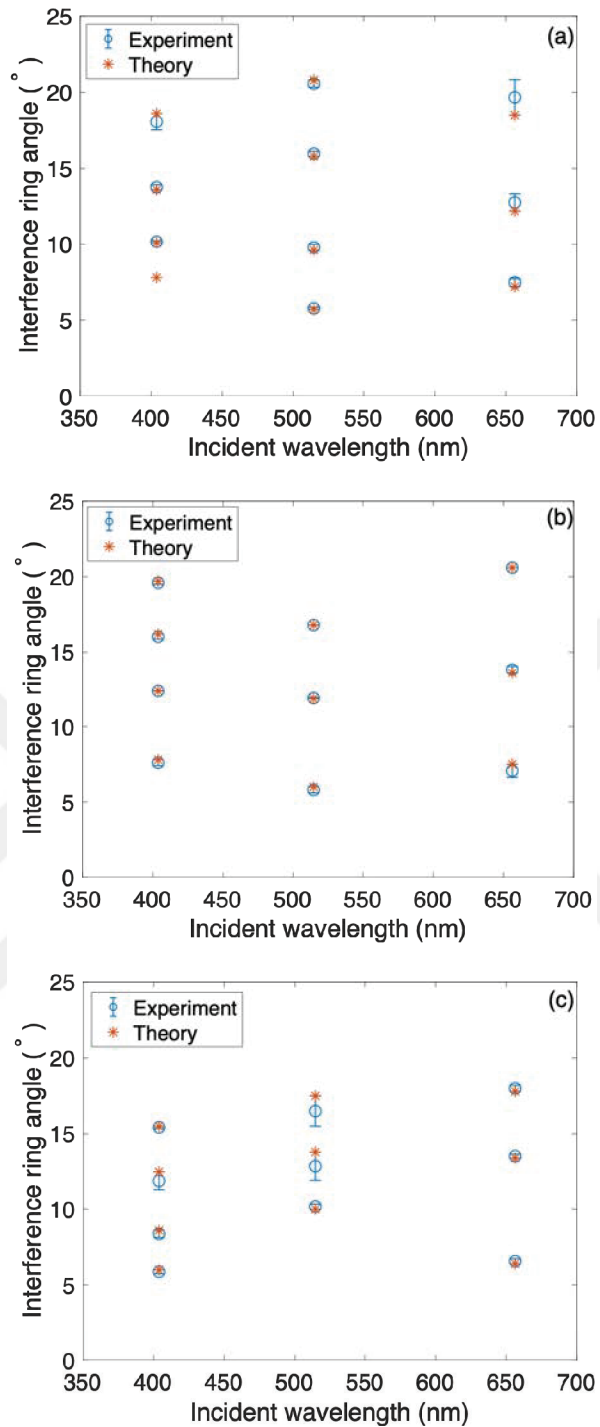
Figure 5.1 Differences between Me8 (a), PS8 (b), and P10 (c) particles at 1.50 fM concentration to monitor consistency between experiments and theory by 656.3 nm, 514.9 nm, and 403.8 nm lasers.

To check the consistency of experimental results at different times (at least 3 months), we prepared sample sets and got scattering images. Once those experiments were completed, we calculated standard deviations between them and got their average to decrease experimental error and use as the final experimental results. Then, mean absolute percentage error and root mean square errors were calculated between the theory

(MATLAB) and experimental results, as shown in Table 5.1. Statistical t-tests showed that there is no meaningful difference between those data.

Table 5.1 Matching of theoretical and three experimental peak angles (P1, P2, P3, P4) with standard deviation and error calculations for red (R), green (G), and blue (B) lasers.

		Theory			Experiment (170 µW)			Experiment (150 µW)			Experiment (160 µW)		
		R	G	B	R	G	B	R	G	B	R	G	B
Me8	P1	7.2	5.7	7.8	7.6	5.9	NA	7.4	5.7	NA	7.4	5.7	NA
	P2	12.2	9.6	10.1	12.8	9.8	10.2	12.7	9.7	10.1	12.8	9.9	10.2
	P3	18.5	15.8	13.6	19.7	16.0	13.6	19.5	15.9	14.0	19.8	16.0	13.7
	P4	NA	20.8	18.6	NA	20.6	18.2	NA	20.6	17.9	NA	20.5	18.1
PS8	P1	7.5	6.0	7.8	6.7	5.8	7.5	7.2	5.7	7.6	7.3	5.9	7.7
	P2	13.6	11.9	12.4	13.9	12.1	12.2	14.0	11.9	12.5	13.6	11.8	12.5
	P3	20.6	16.8	16.2	20.7	16.9	16.0	20.6	16.7	16.1	20.5	16.8	16.0
	P4	NA	NA	19.7	NA	NA	19.6	NA	NA	19.7	NA	NA	19.5
PS10	P1	6.4	10.0	6.0	6.6	10.2	6.0	6.6	10.1	5.7	6.5	10.2	5.9
	P2	13.4	13.8	8.6	13.5	12.5	8.3	13.6	12.9	8.4	13.5	13.2	8.4
	P3	17.8	17.5	12.5	17.9	16.3	11.8	18.1	16.6	11.9	18.0	16.6	12.0
	P4	NA	NA	15.5	NA	NA	15.6	NA	NA	15.4	NA	NA	15.3

		STD			AVEG			MAPE			RMSE		
		R	G	B	R	G	B	R	G	B	R	G	B
Me8	P1	0.12	0.12	NA	7.47	5.77	NA	3.70	1.17	NA	0.28	0.12	NA
	P2	0.06	0.10	0.06	12.77	9.80	10.17	4.64	2.08	0.66	0.57	0.22	0.08
	P3	0.15	0.06	0.21	19.67	15.97	13.77	6.31	1.05	1.23	1.17	0.17	0.24
	P4	NA	0.06	0.15	NA	20.57	18.07	NA	1.12	2.87	NA	0.24	0.55
PS8	P1	0.32	0.10	0.10	7.07	5.80	7.60	5.78	3.33	2.56	0.51	0.22	0.22
	P2	0.21	0.15	0.17	13.83	11.93	12.40	1.72	0.28	0.00	0.29	0.13	0.14
	P3	0.10	0.10	0.06	20.60	16.80	16.03	0.00	0.00	1.03	0.08	0.08	0.17
	P4	NA	NA	0.10	NA	NA	19.60	NA	NA	0.51	NA	NA	0.13
PS10	P1	0.06	0.06	0.15	6.57	10.17	5.87	2.60	1.67	2.22	0.17	0.17	0.18
	P2	0.06	0.35	0.06	13.53	12.87	8.37	1.00	6.76	2.71	0.14	0.98	0.24
	P3	0.10	0.17	0.10	18.00	16.50	11.90	1.12	5.71	4.80	0.22	1.01	0.61
	P4	NA	NA	0.15	NA	NA	15.43	NA	NA	0.43	NA	NA	0.14

5.1 Dataset Creation

After showing the appropriate match between the lab results and theoretical calculations, we created a dataset on MATLAB, and the code for it is given in Appendix B. Using nested for loops of scattering parameters, i.e., particle size, refractive index of the particles and medium, wavelength of incident light, a dataset was created on MATLAB. Considering the limitations of the setup and the literature, we defined appropriate ranges for particle size and refractive indices. For wavelength of incident light, we used the same ones, 656.3 nm, 514.9 nm, and 403.8 nm, as the ones we have in the laboratory. Starting from 5 µm to 13 µm with 0.5 µm increments for particle diameter and from 1.3 to 2.2 with 0.01 increments of refractive index were the ranges of this nested for loop operation. In total, 4641 lines were obtained, including peak angle values (P1, P2, P3, P4) for each combination of loop parameters. A few lines from the dataset are presented in Table 5.2.

Table 5.2 A few sample lines of the dataset created on MATLAB to be used in the Random Forest Algorithm.

Inc. Wl. (nm)	Particle Size	Particle Ref. Index	Medium Ref. Index	P1	P2	P3	P4
403.8	5	2.18	1.3388	7.4	12.6	21.4	0.0
403.8	5	2.19	1.3388	7.4	12.4	21.0	0.0
403.8	5	2.20	1.3388	7.2	12.0	19.7	0.0
403.8	5.5	1.30	1.3388	7.4	12.2	16.7	21.4
403.8	5.5	1.31	1.3388	7.5	12.2	16.8	21.4
403.8	5.5	1.32	1.3388	7.8	12.4	16.8	21.4

Then, we trained two different models, Model 1 for particle size and Model 2 for particle refractive index. We used randomly selected 80% of this primary dataset after adjustments to give it as training data to the model. 20 iterations with 100 trees were used in the model, as commonly done in literature [80]. Once the training had been completed, the remaining part, 20%, was used to test the performance of the model. It is worth saying that, until this step, it was all done using the data created on MATLAB by theoretical calculations.

5.2 Model-1 Particle Size

Modifications were needed on the dataset for each model. For Model 1, particle size estimation, refractive index data were not given as input. Only wavelength of incident

light, the refractive index of the medium (consistent with incident light), and the first four peak angles were used as the input. So, 6 numbers were the input for a line from the dataset, and as seventh, particle size was added, as presented in Appendix C.

After 20 iterations and accuracy calculation for each iteration, the average accuracy was calculated for the final accuracy of the model with test data from the primary dataset.

Figure 5.2 Histogram of the differences between actual and estimated particle size for randomly selected 20% of the dataset.

As presented in Figure 5.2, most of the test results have an error of less than 0.5 μm compared to actual values. The correlation between actual and estimated results is 0.95. Thus, we can say that we trained a successful model to predict particle size from wavelength of incident light, the refractive index of the medium, and the first four bright interference rings of scattering.

Although obtaining promising results by test data created on MATLAB, the critical point is to have the same performance from experimental results as test data. Prediction of particle size will be meaningful if the model successfully determines it. Therefore, we used laboratory results as new test data for Model 1. As given in Table 5.3, among 9 test data, 3 particles by three incident lights, the highest error is 1.5 μm for PS8 by red light. Besides, we only have a 0.5 μm difference between theory and prediction. T-tests also showed no significant difference between those two data types, theory, and prediction. Skewness and kurtosis values for actual data, 0.05 and -1.191, respectively, are acceptable. The same parameters, skewness and kurtosis values, for test data are 0.026 and -1.144, which are also adequate for applying an independent sample t-test. Levene's test for equality of variances' significance value (0.741) demonstrates that the homogeneity of variances condition is met for this data. Assuming equal variances between actual and predicted data for Model 1, the result of the independent sample T-

test in 95% confidence interval shows no statistically significant difference between mean values of actual and predicted data (t=-0.033, df= 1854, $p>0.05$).

Table 5.3 Actual and predicted values of particle sizes for experimental results as test data for Model 1.

	Red (656.3 nm)			Green (514.9 nm)			Blue (403.8 nm)		
	Me8	PS8	PS10	Me8	PS8	PS10	Me8	PS8	PS10
Actual	8 μm	8 μm	10 μm	8 μm	8 μm	10 μm	8 μm	8 μm	10 μm
Predicted	8 μm	6.5 μm	10 μm	8 μm	8 μm	10 μm	8 μm	8 μm	9.5 μm

In summary, our random forest algorithm integrated setup was able to define particle size. We proved that it is possible to do classifications and estimations with a cost-effective, simple, and portable device.

5.3 Model-2 Particle Refractive Index

As modifications on a primary dataset for Model 2, particle refractive index estimation and particle size data were not given as input. Only wavelength of incident light, the refractive index of the medium (consistent with incident light), and the first four peak angles were used as the input. So, 6 numbers were the input for a line from the dataset, and as seventh, particle refractive index was added, as presented in Appendix D.

After 20 iterations and the accuracy calculation for each iteration, the average accuracy was calculated for the final accuracy of the model with test data from the primary dataset.
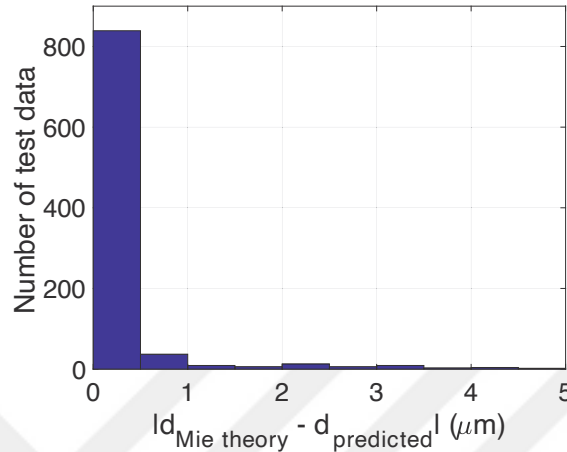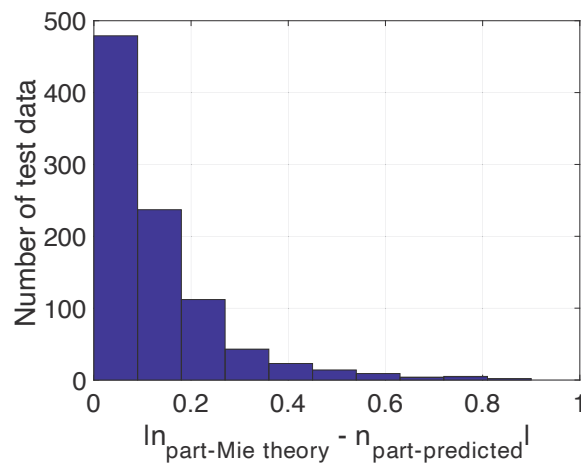

Figure 5.3 Histogram of the differences between actual and estimated particle refractive index for randomly selected 20% of the dataset.

As presented in Figure 5.3, most of the test results have an error of less than 0.5 compared to actual values. The correlation between actual and estimated results is 0.748.

Thus, we trained a successful model to predict particle refractive index from wavelength of incident light, the refractive index of the medium, and the first four bright interference rings of scattering.

Although obtaining promising results by test data created on MATLAB, the important point is having the same performance from experimental results as test data. Prediction of particle refractive index will be meaningful if the model successfully determines it. In addition, this is one of the critical points of this study, considering the estimation of refractive indices of same-sized spheres. Therefore, we used laboratory results as new test data for Model 2. As given in Table 5.4, among 9 test data, 3 particles by three incident lights, the highest error is about 0.13 for PS8 by red light. Other than that, it can be clearly seen that Me8 parameters were estimated identically. PS10 has a better prediction than PS8. T-tests also showed no significant difference between those two data types, theory, and prediction.

Table 5.4 Actual and predicted values of Me8, PS8, and PS10 particle refractive indices by 403.8 nm, 514.9 nm, and 656.3 nm lasers.

	Red (656.3 nm)			Green (514.9 nm)			Blue (403.8 nm)		
	Me8	PS8	PS10	Me8	PS8	PS10	Me8	PS8	PS10
Actual	1.79	1.589	1.589	1.89	1.601	1.601	1.96	1.617	1.617
Predicted	1.79	1.72	1.61	1.89	1.60	1.60	1.96	1.56	1.66

Having appropriate skewness and kurtosis values for Model 2 provided an opportunity to apply an independent sample t-test for this model. Levene's test for equality of variances' significance value (0.711) demonstrates that the homogeneity of variances condition is met for this data. Assuming equal variance between actual and predicted data for Model 2, the result of the independent sample T-test in 95% confidence interval shows no statistically significant difference between mean values of actual and predicted data (t=-0.202, df= 1854, p>0.05).

Chapter 6

Conclusions and Future Prospects

6.1 Conclusions

As stated in the first chapter, the number of microplastics has been increasing dramatically each year due to the careless use of those pollutants' primary and secondary sources. It is not surprising to encounter those particles everywhere. The natural cycle, including water resources, environment, and land we live on, led them to distribute easily. It is difficult to collect and get rid of them once they accumulate, so it is crucial to take precautions at the source. Understanding the material type would help to define the source or track those particles through its center. In addition, there is uncertainty regarding the number of particles made of different materials. A sample may include fewer numbers but more dangerous materials or vice versa. After Egypt, Turkey is the second country releasing the highest amount of microplastic pollutants to the Mediterranean Sea. However, the level of danger in that list has yet to be discovered. The last country in this ranking meaning that it releases the lowest amount, may deliver particles that are more dangerous due to material type with longer lifetime to disappear. Therefore, it is vital to distinguish those particles based on their material type in addition to detecting their size and concentrations.

Light scattering is one of the methods employed to detect and identify microparticles. By just using Snell's Law, using the angle of reflected light, it is possible to have information about particle size. However, a detailed investigation is needed for particle-specific properties in particular materials. Using the refractive index of the particles, which depends on the material itself, scattering patterns can be investigated to acquire more detailed information. This study aimed to use a cost-effective and mobile setup that can record and analyze scattering patterns to classify materials based on their refractive index, size, and concentration.

In the first experiments, it was observed that different materials at different sizes and concentrations give different results when they are irradiated with the laser light at different wavelengths. As expected, an increment in particle size or concentrations makes the forward scattering dominant. In addition, an increment in particle refractive index causes the light to scatter more, resulting in wider scattering angles on scattering patterns. After analysis of those first experiments, it was observed that the angles of the bright interference rings on scattering patterns are particle size, refractive index, and wavelength of incident light specific. However, the change in concentration of a sample did not affect the bright ring angles but the intensity. As expected, the higher number of particles, scatterers, in a sample scattered the light more, and the same but brighter patterns were obtained.

After those observations, experiments using melamine and polystyrene microparticles with 8 and 10 μm sizes were conducted using lasers at three different wavelength of incident lights. All scattering patterns were collected at ten different concentrations, from 0.05 fM to 3.00 fM. After image processing, Me8 and PS8 results were used to analyze material type. As observed, the higher the refractive index of the particle, actually the absolute difference from the refractive index of the medium, resulted in wider scattering angles, as predicted by the theory. In another investigation, the results of PS8 and PS10 particles were used to observe the effect of particle size. The Mie theory states that the forward scattering becomes dominant when particle size increases. Regarding that, as expected Mie resonances, bright ring angles, gathered around zero-degree. Increasing the particle size made the scattering intensity stronger at zero degrees revealing itself as a wider bright spot at the center.

After successfully recording the scattering patterns, we aimed to gather information on particle size and refractive index. For this purpose, we first wrote a code using the Mie scattering equations and compared the theoretical results of the same parameters with the experimental results. Having minor differences provided the opportunity to create a library based on Mie theory and integrate machine learning into the process for fast and accurate analysis of scattering patterns. At this point, nested-for-loops were used for appropriate ranges of particle refractive index, size, and wavelength of incident light. A dataset was created for all combinations. In the first step, 80% of the dataset was randomly selected to train two models, one for particle size and the other for refractive index. The remaining portion, 20%, was applied as test data, and the results were satisfying. The

correlation between actual and estimated results was 0.95 and 0.75 for particle size and refractive index, respectively.

Further investigations were needed to show that the system would also work for real-life applications so that laboratory results were used for the second test data set. The average difference between estimated and actual particle size was 0.23 μm. Out of nine, seven different particle sizes were calculated identically, and the maximum difference was 1.5 μm which belonged to the scattering of the red laser light by PS8 particles.

Regarding the refractive index, which was more challenging to train the model due to having divergence. The refractive index changes with the wavelength of incident light. In addition, different resonance sets at different particle sizes had to give the same particle refractive index value because of a change only in particle size not the material or wavelength of incident light. However, particle size was not used as an input of the algorithm. This made the process complex to learn for the algorithm. However, especially Me8 parameters were calculated successfully. The average difference for the refractive index turned out to be 0.015. The highest difference was 0.13 for PS8 particles when the red laser was employed.

In conclusion, the systems successfully distinguished particle size and refractive index for particle classification. Integrating a random forest algorithm, which is easy and appropriate for this problem, provided fast characterization of scattering patterns regarding particles' physical properties. Having a device that is portable, cost-effective, durable, and easy to use would provide an opportunity for further developments regarding the research that has been done in this field. Furthermore, the shape of the scatterers or the detection range can be modified with minor adjustments, *i.e.*, adding lenses or additional cameras.

6.2 Societal Impact and Contribution to Global Sustainability

The societal impact of microplastics is significant. The increasing amount of microplastics in our environment has raised public awareness of the plastic pollution problem and has led to calls for action from consumers, businesses, and governments. People are becoming more conscious of plastic use and actively seeking alternative solutions. Furthermore, companies are also changing their practices and developing

sustainable packaging alternatives. However, the problem of microplastics requires a global effort to mitigate its impact.

The issue of microplastics is closely linked to the United Nations' Sustainable Development Goals (SDGs). SDG 14, Life Below Water, specifically aims to conserve and sustainably use the oceans, seas, and marine resources for sustainable development. Microplastics have been identified as a significant threat to marine ecosystems, and addressing the issue is crucial to achieving SDG 14.

Furthermore, microplastics also have implications for other SDGs. For example, SDG 12, Responsible Consumption and Production, emphasizes the need for sustainable consumption and production patterns to minimize waste generation and reduce the negative impacts of consumption on the environment. Addressing microplastics requires a shift towards sustainable consumption and production patterns that prioritize reducing plastic use and promoting proper waste management practices. Moreover, microplastics can affect human health, which is addressed by SDG 3, Good Health and Well-being. It is essential to address the issue of microplastics to protect both marine and human health.

In conclusion, addressing the issue of microplastics is crucial in achieving multiple SDGs. It requires a global effort to reduce plastic use, promote sustainable consumption and production patterns, and develop effective waste management systems. By addressing the issue of microplastics, we can promote a more sustainable and healthy future for our planet and its inhabitants. Governments and organizations must work together to address this issue and develop policies and initiatives to reduce plastic use and improve waste management systems. Working together can create a more sustainable future for our planet.

6.3 Future Prospects

In this study, the setup can be used for different samples, *i.e.,* DNAs, bacteria, cells, metallic particles, etc. A thin lens may be needed to focus light on a much smaller area to investigate nano-size particles. In addition, by using appropriate solvents, solid samples can be diluted and examined after some filtering and basic preprocessing steps.

Microplastics are expected to continue to be a major concern as plastic production and consumption continue to increase globally. However, there are also promising prospects for addressing the issue and detecting environmental microplastics. To address the issue, there is growing awareness among consumers, businesses, and governments

about the negative impacts of microplastics on the environment and human health. This has led to a push for reducing plastic use and improving waste management systems. Additionally, ongoing research on sustainable alternatives to plastic and innovative technologies for capturing and removing microplastics from the environment exists.

There have been advancements in analytical methods for identifying and quantifying microplastics in different environmental samples. These include Raman spectroscopy, Fourier-transform infrared spectroscopy, and pyrolysis-gas chromatography-mass spectrometry. Furthermore, there is ongoing research into developing more efficient and cost-effective methods for detecting microplastics, such as biosensors and microfluidic devices.

Overall, the microplastics issue and detection prospects are both challenging and promising. Addressing the issue will require a concerted effort from individuals, businesses, and governments to reduce plastic use, improve waste management systems, and invest in sustainable alternatives. At the same time, ongoing research into detection technologies will be crucial in identifying the extent of the problem and developing effective mitigation strategies.

BIBLIOGRAPHY

[1] E. J. Carpenter and K. L. Smith, "Plastics on the Sargasso Sea surface," Science (1979), 175, 1240–1241 (1972).

[2] E. J. Carpenter, S. J. Anderson, G. R. Harvey, H. P. Miklas, and B. B. Peck, "Polystyrene spherules in coastal waters," Science (1979), 178, 749–750 (1972).

[3] A. Ashkin, "Acceleration and trapping of particles by radiation pressure," Phys Rev Lett, 24, 156 (1970).

[4] J. A. Ivar Do Sul and M. F. Costa, "The present and future of microplastic pollution in the marine environment," Environmental Pollution, 185, 352–364 (2014).

[5] S. L. Wright, R. C. Thompson, and T. S. Galloway, "The physical impacts of microplastics on marine organisms: a review.," Environ Pollut, 178, 483–492 (2013).

[6] B. E. Oßmann, G. Sarau, H. Holtmannspötter, M. Pischetsrieder, S. H. Christiansen, and W. Dicke, "Small-sized microplastics and pigmented particles in bottled mineral water," Water Res, 141, 307–316 (2018).

[7] A. Dick Vethaak and J. Legler, "Microplastics and human health," Science (1979), 371, 672–674 (2021).

[8] K. D. Cox, G. A. Covernton, H. L. Davies, J. F. Dower, F. Juanes, and S. E. Dudas, "Human consumption of microplastics," Environ Sci Technol, 53, 7068–7074 (2019).

[9] D. Schymanski, C. Goldbeck, H. U. Humpf, and P. Fürst, "Analysis of microplastics in water by micro-Raman spectroscopy: Release of plastic particles from different packaging into mineral water," Water Res, 129, 154–162 (2018).

[10] Richard Kirby, "The Nitty Gritty on Microplastics,"
<https://whalewatchingauckland.com/blog/the-nitty-gritty-on-microplastics/>
(29 April 2023).

[11] Per Harald Olsen, NTNU, "Water flea (Daphnia magna Straus),"
<https://www.artsdatabanken.no/Taxon/Daphnia%20magna/123935> (29 April 2023).

[12] A. Isobe, S. Iwasaki, K. Uchida, and T. Tokai, "Abundance of non-conservative microplastics in the upper ocean from 1957 to 2066," Nature Comm, 10:1 10, 1–13 (2019).

[13] K. E. Peiponen, J. Räty, U. Ishaq, S. Pélisset, and R. Ali, "Outlook on optical identification of micro- and nanoplastics in aquatic environments," Chemosphere, 214, 424–429 (2019).

[14] M. F. Costa, J. A. Ivar Do Sul, J. S. Silva-Cavalcanti, M. C. B. Araújo, Â. Spengler, and P. S. Tourinho, "On the importance of size of plastic fragments and pellets on the strandline: A snapshot of a Brazilian beach," Environ Monit Assess, 168, 299–304 (2010).

[15] A. Tahir, M. F. Samawi, K. Sari, R. Hidayat, R. Nimzet, E. A. Wicaksono, L. Asrul, and S. Werorilangi, "Studies on microplastic contamination in seagrass beds at Spermonde Archipelago of Makassar Strait, Indonesia," J Phys Conf Ser, 1341, 022008 (2019).

[16] P. K. Cheung and L. Fok, "Evidence of microbeads from personal care product contaminating the sea," Mar Pollut Bull ,109, 582–585 (2016).

[17] S. Sridharan, M. Kumar, L. Singh, N. S. Bolan, and M. Saha, "Microplastics as an emerging source of particulate air pollution: A critical review," J Hazard Mater, 418, 126245 (2021).

[18] P. Orellano, J. Reynoso, N. Quaranta, A. Bardach, and A. Ciapponi, "Short-term exposure to particulate matter (PM10 and PM2.5), nitrogen dioxide (NO2), and ozone (O3) and all-cause and cause-specific mortality: Systematic review and meta-analysis," Environ Int, 142 (2020).

[19] "Microplastics and Their Impacts on Organisms and Trophic Chains," <https://www.mdpi.com/journal/water/special_issues/Microplastics_Impacts#info> (29 April 2023).

[20] E. A. Shore, J. A. deMayo, and M. H. Pespeni, "Microplastics reduce net population growth and fecal pellet sinking rates for the marine copepod, Acartia tonsa," Environmental Pollution, 284, 117379 (2021).

[21] O. Olatunji, "Microplastics: Emerging issues in emerging urbanization," in *Plastic and polymer industry by region*, O. Olatunji (Ed.), 177-199, Springer, (2022)

[22] P. M. Potter, "Microplastics: emerging trends and research gaps," ACS Spring 2021 National Meeting (2021).

[23] L. G. A. Barboza, A. Dick Vethaak, B. R. B. O. Lavorante, A. K. Lundebye, and L. Guilhermino, "Marine microplastic debris: An emerging issue for food security, food safety and human health," Mar Pollut Bull, 133, 336–348 (2018).

[24] C. Rubio-Armendáriz, S. Alejandro-Vega, S. Paz-Montelongo, Á. J. Gutiérrez-Fernández, C. J. Carrascosa-Iruzubieta, and A. Hardisson-de la Torre, "Microplastics as emerging food contaminants: A challenge for food safety," Int J Environ Res Public Health, 19 (2022).

[25] S. A. Mason, V. G. Welch, and J. Neratko, "Synthetic polymer contamination in bottled water," Front Chem, 6, 407 (2018).

[26] J. Barrett, Z. Chase, J. Zhang, M. M. B. Holl, K. Willis, A. Williams, B. D. Hardesty, and C. Wilcox, "Microplastic pollution in deep-sea sediments from the Great Australian Bight," Front Mar Sci, 7, 808 (2020).

[27] J. Vieira Dantas Filho, V. Perez Pedroti, B. L. Temponi Santos, M. M. de Lima Pinheiro, Á. Bezerra de Mira, F. Carlos da Silva, E. C. Soares e Silva, J. Cavali, E. A. Cecilia Guedes, et al., "First evidence of microplastics in freshwater from fish farms in Rondônia state, Brazil," Heliyon, 9, e15066 (2023).

[28] Blazej Kupec, "What is Microfiber Pollution and How Can We Stop It," <https://blog.planetcare.org/what-is-microfiber-pollution-and-how-can-we-stop-it/> (29 April 2023).

[29] N. N. Boustany, S. A. Boppart, and V. Backman, "Microscopic imaging and spectroscopy with scattered light," Annu Rev Biomed Eng, 12, 285 (2010).

[30] A. Scircle and J. V. Cizdziel, "Detecting and quantifying microplastics in bottled water using fluorescence microscopy: A new experiment for instrumental analysis and environmental chemistry courses," J Chem Educ, 97, 234–238 (2020).

[31] F. Merola, P. Memmolo, V. Bianco, M. Paturzo, M. G. Mazzocchi, and P. Ferraro, "Searching and identifying microplastics in marine environment by digital holography⋆," The European Physical Journal Plus, 133:9 133, 1–6 (2018).

[32] Y. Chen, D. Wen, J. Pei, Y. Fei, D. Ouyang, H. Zhang, and Y. Luo, "Identification and quantification of microplastics using Fourier-transform infrared spectroscopy: Current status and future prospects," Curr Opin Environ Sci Health, 18, 14–19 (2020).

[33] N. Kaile, M. Lindivat, J. Elio, G. Thuestad, Q. G. Crowley, and I. A. Hoell, "Preliminary results from detection of microplastics in liquid samples using flow cytometry," Front Mar Sci, 7, 856 (2020).

[34] S. Veerasingam, M. Ranjani, R. Venkatachalapathy, A. Bagaev, V. Mukhanov, D. Litvinyuk, M. Mugilarasan, K. Gurumoorthi, L. Guganathan, et al., "Contributions of Fourier transform infrared spectroscopy in microplastic pollution research: A review," Critical Reviews in Environmental Science and Technology, 51, 2681–2743 (2020).

[35] A. H. Iri, M. H. A. Shahrah, A. M. Ali, S. A. Qadri, T. Erdem, I. T. Ozdur, and K. Icoz, "Optical detection of microplastics in water," Environmental Science and Pollution Research, 28, 63860–63866 (2021).

[36] S. Oh, H. Hur, Y. Kim, S. Shin, H. Woo, J. Choi, and H. H. Lee, "Peptide specific nanoplastic detection based on sandwich typed localized surface plasmon resonance," Nanomaterials, 11, 2887 (2021).

[37] J. Shan, J. Zhao, Y. Zhang, L. Liu, F. Wu, and X. Wang, "Simple and rapid detection of microplastics in seawater using hyperspectral imaging technology," Anal Chim Acta, 1050, 161–168 (2019).

[38] C. K. Chen, J. Zhang, A. Bhingarde, T. Matotek, J. Barrett, B. D. Hardesty, M. M. Banaszak Holl, and B. L. Khoo, "A portable purification system for the rapid removal of microplastics from environmental samples," Chemical Engineering Journal, 428, 132614 (2022).

[39] X. Zhang, H. Zhang, K. Yu, N. Li, Y. Liu, X. Liu, H. Zhang, B. Yang, W. Wu, et al., "Rapid monitoring approach for microplastics using portable Pyrolysis-Mass spectrometry," Anal Chem, 92, 4656–4662 (2020).

[40] B. O. Asamoah, B. Kanyathare, M. Roussey, and K. E. Peiponen, "A prototype of a portable optical sensor for the detection of transparent and translucent microplastics in freshwater," Chemosphere, 231, 161–167 (2019).

[41] R. L. Coppock, M. Cole, P. K. Lindeque, A. M. Queirós, and T. S. Galloway, "A small-scale, portable method for extracting microplastics from marine sediments," Environmental Pollution, 230, 829–837 (2017).

[42] V. Nava and B. Leoni, "A critical review of interactions between microplastics, microalgae and aquatic ecosystem function," Water Res, 188, 116476 (2021).

[43] S. Kacprzak and L. D. Tijing, "Microplastics in indoor environment: Sources, mitigation and fate," J Environ Chem Eng, 10, 107359 (2022).

[44] M. Pittroff, Y. K. Müller, C. S. Witzig, M. Scheurer, F. R. Storck, and N. Zumbülte, "Microplastic analysis in drinking water based on fractionated filtration sampling and Raman microspectroscopy," Environmental Science and Pollution Research, 28, 59439–59451 (2021).

[45] J. Masura, J. Baker, G. Foster, and C. Arthur, "Laboratory methods for the analysis of microplastics in the marine environment: Recommendations for quantifying synthetic particles in waters and sediments," Siver Spring, MD, NOAA Marine Debris Division, 31, (2015).

[46] L. Xie, K. Gong, Y. Liu, and L. Zhang, "Strategies and challenges of identifying nanoplastics in environment by Surface-Enhanced Raman spectroscopy," Environ Sci Technol, 57, 25–43 (2023).

[47] S. K. Brar and M. Verma, "Measurement of nanoparticles by light-scattering techniques," TrAC Trends in Analytical Chemistry, 30, 4–17 (2011).

[48] A. R. Petosa, D. P. Jaisi, I. R. Quevedo, M. Elimelech, and N. Tufenkji, "Aggregation and deposition of engineered nanomaterials in aquatic environments: Role of physicochemical interactions," Environ Sci Technol, 44, 6532–6549 (2010).

[49] C. F. Bohren and D. R. Huffman, *Absorption and scattering of light by small particles,* Wiley, (1983).

[50] J. R. Frisvad, N. J. Christensen, and H. W. Jensen, "Predicting the apperance of materials using Lorenz-Mie theory," in *The Mie Theory: Basics and Applications,* W. Hergert and T. Wriedt, (Eds.), 101-133, Springer, (2012).

[51] "Light Scattering – PhysicsOpenLab,"
<https://physicsopenlab.org/2019/07/10/light-scattering/> (5 July 2023).

[52] M. J. Cooper, "Compton scattering and electron momentum determination," Reports on Progress in Physics, 48, 415 (1985).

[53] R. Van Boxem, B. Partoens, and J. Verbeeck, "Rutherford scattering of electron vortices," Phys Rev A, 89, 032715 (2014).

[54] A. Donnachie and P. V. Landshoff, "Dynamics of elastic scattering," Nucl Phys B, 267, 690–701 (1986).

[55] J. Blümlein, "The theory of deeply inelastic scattering," Prog Part Nucl Phys, 69, 28–84 (2013).

[56] B. Berne and R. Pecora, "*Dynamic light scattering: With applications to chemistry, biology, and physics*", Dover Publications, (2000).

[57] I. Kolokolnikov, E. Nepomnyashchaya, and E. Velichko, "Static light scattering for determination of physical parameters of macro- and nanoparticles," J Phys Conf Ser, 1410, 012168 (2019).

[58] R. Xu, "Light scattering: A review of particle characterization applications," Particuology, 18, 11–21 (2015).

[59] J. R. Frisvad, "Application of Lorenz-Mie theory in graphics," 26-28, in "Mie Theory 1908-2008: Present developments and interdisciplinary aspects of light scattering," in *The Mie theory: Basics and applications,* W. Hergert and T. Wriedt, (Eds.), 1-51, Springer, (2012).

[60] H. C. van de Hulst, *Light scattering by small particles*, Dover Publications, (1981).

[61] D. W. Hahn, "Light scattering theory" (2009).

[62] T. Wriedt, "Mie theory: A review," in *The Mie theory: Basics and applications,* W. Hergert and T. Wriedt, (Eds.), 53-71, Springer, (2012).

[63] W. Hergert, "Gustav Mie: From electromagnetic scattering to an electromagnetic view of matter," in *The Mie theory: Basics and applications,* W. Hergert and T. Wriedt, (Eds.), 1-51, Springer, (2012).

[64] Z. Liu, L. Li, H. Li, and L. Mei, "Preliminary studies on atmospheric monitoring by employing a portable unmanned Mie-scattering scheimpflug lidar system," Remote Sensing, 11, 837 (2019).

[65] Y. Le Pan, K. Aptowicz, J. Arnold, S. Cheng, A. Kalume, P. Piedra, C. Wang, J. Santarpia, and G. Videen, "Review of elastic light scattering from single aerosol particles and application in bioaerosol detection," J Quant Spectrosc Radiat Transf, 279, 108067 (2022).

[66] B. Y. Shekunov, P. Chattopadhyay, H. H. Y. Tong, and A. H. L. Chow, "Particle size analysis in pharmaceutics: Principles, methods and applications," Pharm Res, 24, 203–227 (2007).

[67] P. H. Kaye, K. Aptowicz, R. K. Chang, V. Foot, and G. Videen, "Angularly resolved elastic scattering from airborne particles: Potential for characterizing, classifying, and identifying individual aerosol particles," Optics of Biological Particles, 31–61 (2007).

[68] Q. Fu and W. Sun, "Mie theory for light scattering by a spherical particle in an absorbing medium," Appl Opt, 40, 1354 (2001).

[69] N. G. Khlebtsov, "Extinction and scattering of light by nonspherical plasmonic particles in absorbing media," J Quant Spectrosc Radiat Transf, 280, 108069 (2022).

[70] G. Gouesbet, "Latest achievements in generalized Lorenz-Mie theories: A commented reference database," Ann Phys, 526, 461–489 (2014).

[71] I. R. Ciric and F. R. Cooray, "Theoretical and numerical techniques" in *Light scattering by nonspherical particles: Theory, measurements, and applications* (M. I. Mishchenko, J. W. Hovenier, and L. D. Travis (Eds.), Academic Press, (2000).

[72] I. Kabakova, G. Scarcelli, and S. H. Yun, "Brillouin light scattering in biological systems," Semiconductors and Semimetals, 110, 313–348 (2022).

[73] F. L. Pedrotti, L. M. Pedrotti, and L. S. Pedrotti, *Introduction to optics, 3rd Edition,* Cambridge University Press, (2018).

[74] E. Hecht, *Optics*, 5th Edition, Pearson, (2017).

[75] A. Karami, A. Golieskardi, C. Keong Choo, V. Larat, T. S. Galloway, and B. Salamatinia, "The presence of microplastics in commercial salts from different countries," Scientific Reports, 7:1 7, 1–11 (2017).

[76] B. Balogun and A. Timothy, "Production and characterization of melamine-formaldehyde moulding powder," in International Journal of Advanced Academic Research | Sciences, 6 (2020).

[77] Physical constants of organic compounds, *CRC Handbook of chemistry and physics* W. M. Haynes (Ed.)," 97th Edition, CRC Press, (2016).

[78] "Melamine," <https://www.chembk.com/en/chem/Melamine> (29 April 2023).

[79] J. L. Speiser, M. E. Miller, J. Tooze, and E. Ip, "A comparison of Random Forest variable selection methods for classification prediction modeling," Expert Syst Appl, 134, 93–101 (2019).

[80] G. Biau and E. Scornet, "A Random Forest guided tour," Test, 25, 197–227 (2016).

[81] M. Z. Joharestani, C. Cao, X. Ni, B. Bashir, and S. Talebiesfandarani, "PM2.5 prediction based on Random Forest, XGBoost, and Deep Learning using multisource remote sensing data," Atmosphere, 10, 373 (2019).

[82] "Random Forest ist ein Open-Source-Algorithmus, der funktioniert," <https://nara.getarchive.net/de/media/random-forest-is-an-open-source-algorithm-that-functions-6cecd3> (5 July 2023).

APPENDIX A

Code for Scattering

```
d=8e-6;        %sphere diameter
m_sph=1.79;      %sphere refractive index
m_env=1.331;     %medium refractive index
l_vac=656.3e-9;  %wavelength in vacuum

%H20:  1.3310R, 1.3344G, 1.3388B
%ME:   1.79-R, 1.89-G, 1.96-B
%PS:   1.589-R, 1.601-G, 1.617-B


%%%%%%%%%% CALCULATIONS START AFTER HERE
%%%%%%%%%%%%%%%%%%%%
a=d/2;
k=2*pi/(l_vac/m_env);
x=k*a;%DWH eq.1
m=m_sph/m_env;

M=ceil(x + 4*(x^(1/3) + 2));
n=1:M;

fpsi=sqrt(pi*x/2)*besselj(n+0.5,x); %eq 4.9 %DWH eq.29
dfb=0.5*(besselj(n-0.5,x)-besselj(n+1.5,x));
dfpsi=0.5*sqrt((pi/2)/x)*besselj(n+0.5,x)+sqrt(pi*x/2)*dfb;

fpsim=sqrt(pi*(m*x)/2)*besselj(n+0.5,m*x);
fdbm=0.5*(besselj(n-0.5,m*x)-besselj(n+1.5,m*x));
fdpsim=0.5*sqrt((pi/2)/(m*x))*besselj(n+0.5,m*x)+sqrt(pi*(m*x)/2)*fdbm;

fxsi=sqrt(pi*x/2)*besselh(n+0.5,x); %eq 4.10 %DWH eq.30
fdh=0.5*(besselh(n-0.5,x)-besselh(n+1.5,x));
fdxsi=0.5*sqrt((pi/2)/x)*besselh(n+0.5,x)+sqrt(pi*x/2)*fdh;

an=(fpsi.*fdpsim-m*fpsim.*dfpsi)./(fxsi.*fdpsim-m*fpsim.*fdxsi); %eq 4.56 %DWH
eq.26
bn=(m*fpsi.*fdpsim-fpsim.*dfpsi)./(m*fxsi.*fdpsim-fpsim.*fdxsi); %eq 4.57 %DWH
eq.27
```

```matlab
text=(l_vac/m_env)^2/(2*pi)*sum((2*n+1).*real(an+bn)); %total ext cs %eq 4.62
%DWH eq.32
tscat=(l_vac/m_env)^2/(2*pi)*sum((2*n+1).*(abs(an).^2+abs(bn).^2)); %total scat cs
%eq 4.61 %DWH eq.33
tabsorp=text-tscat; %total abs cs

theta=0:0.1:25;
fpi=zeros(length(n),length(theta));
ftau=zeros(length(n),length(theta));
mu=cosd(theta);

%calculated by the info given between eq.4.47 and 4.48
%fpi(0)=0;
%fpi(1)=1;
fpi(1,:)=1;
fpi(2,:)=3*mu;
ftau(1,:)=mu;
ftau(2,:)=6*mu.^2 - 3;

for n2=3:M
    fpi(n2,:)=(2*n2-1)/(n2-1)*mu.*fpi(n2-1,:)-n2/(n2-1).*fpi(n2-2,:); %eq 4.47
    ftau(n2,:)=n2*mu.*fpi(n2,:)-(n2+1)*fpi(n2-1,:); %eq 4.48
end

En=(2*n+1)./(n.*(n+1)); %DWH eq.22
aif0=abs(En.*an*fpi+En.*bn*ftau).^2; %DWH eq.22
aif90=abs(En.*an*ftau+En.*bn*fpi).^2; %DWH eq.23

m_air=1;
dscat0=(l_vac/m_env)^2/(4*pi^2)*aif0; % diff scat cs (parallel) %DWH eq.19
dscat90=(l_vac/m_env)^2/(4*pi^2)*aif90; % diff scat cs (perpendicular) %DWH eq.20
dscat=(dscat0+dscat90)/2; % diff scat cs (unpolarized) %DWH eq.21

theta2=asind(sind(theta)*m_env/m_air);

plim=find(theta2(:)>=5&theta2(:)<=21); %between 5-21 degree
[aa,bb]=findpeaks(dscat(plim));
peaks=round(theta2(bb+plim(1)),1); %calculation of peak angle

plot(theta2(plim),dscat(plim)./max(dscat(plim)),'LineWidth',2,'Color','r','LineStyle','-');
%title('Unpolarised');
xlabel('Scattering Angle ( ^\circ )','FontSize',16)
ylabel('Differential scattering cross section (A.U.)','FontSize',16)
xlim([theta2(plim(1)) theta2(plim(end))]); hold on
xlim([5 22])
ylim([0 1])

lmb=char(hex2dec('039B'));
fprintf(['Peaks at;\n' 'Diameter(um): ', num2str(d*1e+6), '\n' ...
      lmb '(nm): ' num2str(l_vac*1e+9) '\n' ...
```

```
'n_sphere: ', num2str(m_sph), [', and \n' ...
'n_medium: '], num2str(m_env) ' = [',num2str(peaks) ']\n']) %??
```

OUTPUT:

Peaks at;

Diameter(um): 8

Λ(nm): 656.3

n_sphere: 1.79, and

n_medium: 1.331 = [7.2   12.2   18.5]
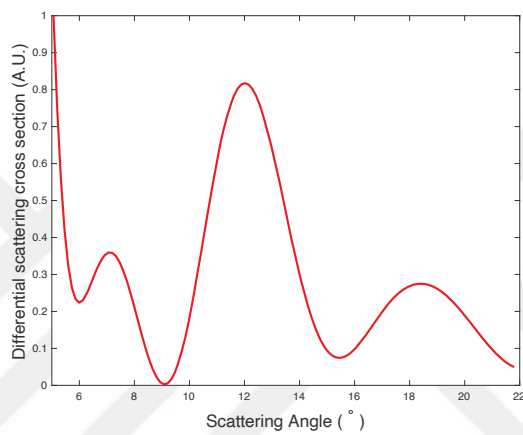
Figure A.1 Theoretical result of angular scattering of Me8 particles by 656.3 nm laser.

APPENDIX B

Code for Dataset Creation

```matlab
clear
clc

line=0;
wl=[656.3 514.9 403.8];
rad=5:0.5:13;
nparticle=1.3:0.01:2.2;
nmed=[1.331 1.3344 1.3388];

%H20: 1.3310R, 1.3344G, 1.3388B
%ME:  1.79-R, 1.89-G, 1.96-B
%PS:  1.589-R, 1.601-G, 1.617-B

for i1=1:length(wl)
for i2=1:length(rad)
for i3=1:length(nparticle)

    line=line+1;

    [a(line,:),theta,theta2]=mie(wl(i1),rad(i2),nparticle(i3),nmed(i1));

    dta(line,1)=wl(i1);
    dta(line,2)=rad(i2);
    dta(line,3)=nparticle(i3);
    dta(line,4)=nmed(i1);


end
end
end
```

APPENDIX C

Sample dataset for Model 1

Table C.1 Sample lines from dataset adjusted for training for Model 1.

	Incident wl (nm)	n_med	p1	p2	p3	p4	d_part (µm)
1	403.8	1.3388	8.2	13.4	18.5	0.0	5
2	403.8	1.3388	8.4	13.6	18.5	0.0	5
3	403.8	1.3388	8.6	13.6	18.5	0.0	5
4	403.8	1.3388	8.6	13.6	18.5	0.0	5
5	403.8	1.3388	8.6	13.6	18.5	0.0	5
6	403.8	1.3388	8.6	13.6	18.3	0.0	5
…	…	…	…	…	…	…	…
1545	403.8	1.3388	6.6	8.2	10.1	13.3	13
1546	403.8	1.3388	6.6	8.4	12.0	15.2	13
1547	403.8	1.3388	6.7	8.3	10.6	11.4	13
1548	514.9	1.3344	10.7	17.3	0.0	0.0	5
1549	514.9	1.3344	10.8	17.5	0.0	0.0	5
1550	514.9	1.3344	11.0	17.5	0.0	0.0	5
…	…	…	…	…	…	…	…
3092	514.9	1.3344	6.1	8.2	10.8	15.2	13
3093	514.9	1.3344	6.1	8.3	10.6	14.8	13
3094	514.9	1.3344	6.0	8.4	10.2	13.0	13
3095	656.3	1.331	13.9	0.0	0.0	0.0	5
3096	656.3	1.331	14.0	0.0	0.0	0.0	5
3097	656.3	1.331	14.0	0.0	0.0	0.0	5
…	…	…	…	…	…	…	…
4636	656.3	1.331	7.7	10.4	14.3	19.2	13
4637	656.3	1.331	7.9	10.1	13.6	18.8	13
4638	656.3	1.331	7.7	13.2	17.4	0.0	13
4639	656.3	1.331	7.6	11.1	16.6	21.5	13
4640	656.3	1.331	7.6	10.7	16.1	20.2	13
4641	656.3	1.331	7.7	10.5	14.3	19.5	13

APPENDIX D

Sample dataset for Model 2

Table D.1 Sample lines from dataset adjusted for training for Model 2.

	Incident wl (nm)	n_med	p1	p2	p3	p4	n_part (μm)
1	403.8	1.3388	8.2	13.4	18.5	0.0	1.30
2	403.8	1.3388	8.4	13.6	18.5	0.0	1.31
3	403.8	1.3388	8.6	13.6	18.5	0.0	1.32
4	403.8	1.3388	8.6	13.6	18.5	0.0	1.33
5	403.8	1.3388	8.6	13.6	18.5	0.0	1.34
6	403.8	1.3388	8.6	13.6	18.3	0.0	1.35
…	…	…	…	…	…	…	…
1545	403.8	1.3388	6.6	8.2	10.1	13.3	2.18
1546	403.8	1.3388	6.6	8.4	12.0	15.2	2.19
1547	403.8	1.3388	6.7	8.3	10.6	11.4	2.20
1548	514.9	1.3344	10.7	17.3	0.0	0.0	1.30
1549	514.9	1.3344	10.8	17.5	0.0	0.0	1.31
1550	514.9	1.3344	11.0	17.5	0.0	0.0	1.32
…	…	…	…	…	…	…	…
3092	514.9	1.3344	6.1	8.2	10.8	15.2	2.18
3093	514.9	1.3344	6.1	8.3	10.6	14.8	2.19
3094	514.9	1.3344	6.0	8.4	10.2	13.0	2.20
3095	656.3	1.331	13.9	0.0	0.0	0.0	1.30
3096	656.3	1.331	14.0	0.0	0.0	0.0	1.31
3097	656.3	1.331	14.0	0.0	0.0	0.0	1.32
…	…	…	…	…	…	…	…
4636	656.3	1.331	7.7	10.4	14.3	19.2	2.15
4637	656.3	1.331	7.9	10.1	13.6	18.8	2.16
4638	656.3	1.331	7.7	13.2	17.4	0.0	2.17
4639	656.3	1.331	7.6	11.1	16.6	21.5	2.18
4640	656.3	1.331	7.6	10.7	16.1	20.2	2.19
4641	656.3	1.331	7.7	10.5	14.3	19.5	2.20

APPENDIX E

Code for Random Forest algorithm

```
clear
close all
warning off
data=readtable('lib_np.xlsx');
%data2=readtable('lab_np.xlsx'); %use when lab results will be tested
prm='np'; %model type

for i=1:20
i
cv = cvpartition(size(data,1),'HoldOut',0.2); %%20 of data is separated for testing
idx = cv.test;
dataTrain=data(~idx,:);
dataTest=data(idx,:);
%dataTest=data2; %use when lab results will be tested
testing=dataTest(1:end,1:end-1);
model1=fitensemble(dataTrain,prm,'Bag',100,'Tree','Type','classification');
prediction1=predict(model1,testing);
ms1(i)=(sum(prediction1==table2array(dataTest(:,end)))/size(dataTest,1))*100;

end

accuracy=sum(ms1)/i;
sdev=std(ms1);


fprintf(['Mean of testing ' prm ' values:' num2str(mean(dataTest{:,7})) '\n']);
fprintf(['Mean of predicted ' prm ' values:' num2str(mean(prediction1)) '\n']);
```

CURRICULUM VITAE

2007 – 2012	B.Sc., Electrical and Electronics Engineering, Sakarya University, Sakarya, TURKEY
2015 – 2016	M.Sc., Electrical and Computer Engineering, Abdullah Gül University, Kayseri, TURKEY
2017 – 2023	Ph.D., Electrical and Computer Engineering, Abdullah Gül University, Kayseri, TURKEY

SELECTED PUBLICATIONS AND PRESENTATIONS

J1) S. Genc, T. Erdem, K. Icoz*, "Size, Material Type and Concentration Estimation for Micro-Particles in Liquid Samples", (June 2023 - Submitted)

J2) S. Genc, K. Icoz, T. Erdem*, "Numerical Analysis for Size, Refractive Index, and Wavelength Dependence of Optical Scattering by Microplastics and Experimental Verification", Royal Society Open Science, (July 2023)

J3) S. Genc, M. Uguz, O. Yilmaz, E. Mutlugun*, "Rec.2100 Color Gamut Revelation Using Spectrally Ultra-Narrow Emitters", Optical Engineering, (Nov. 2017)

C1) S. Genc, K. Icoz, T. Erdem, "Machine Learning Based Classification of Microparticles Using Optical Scattering Simulations", 16th Nanoscience and Nanotechnology Conference (NANOTR), Ankara, Turkey. (Sept. 2022)

C2) S. Genc, K. Icoz, T. Erdem, "Machine Learning Assisted Particle Size and Type Classification Using Wavelength-Dependent Scattering Patterns", International Conference on Optics and Photonics 2021 (OPTO2021), Wroclaw, Poland. (July 2021)

T.C.
ABDULLAH GÜL ÜNİVERSİTESİ
Fen Bilimleri Enstitüsü

ENSTİTÜ YÖNETİM KURULU KARARLARI

Toplantı Tarihi	Toplantı Sayısı	Karar Sayısı
17/08/2023	26	1…4.

Karar No 3: 2022-2023 Eğitim Öğretim Yılı Bahar Yarıyılında Enstitümüzden mezun olan öğrencinin tezinin **erişime kısıtlanması** hakkında görüşüldü.

Yükseköğretim Kurulu Başkanlığı'nın Lisansüstü Tezlerin Elektronik Ortamda Toplanması, Düzenlenmesi ve Erişime Açılmasına İlişkin Yönergesinin 6/2. maddesi uyarınca aşağıda bilgileri bulunan mezun durumdaki öğrencinin tezinin "Yeni teknik, materyal ve metotların kullanıldığı, henüz makaleye dönüşmemiş veya patent gibi yöntemlerle korunmamış ve internetten paylaşılması durumunda 3. şahıslara veya kurumlara haksız kazanç imkânı oluşturabilecek bilgi ve bulguları içermesi" nedeniyle **6 (altı) ay erişime kısıtlanmasına** oy birliği ile karar verilmiştir.

Kısıtlama Talebinde Bulunan Öğrencinin					
Adı Soyadı	**Numarası**	**T.C. Kimlik No**	**Anabilim Dalı**	**Programı**	**Mezuniyet Tarihi**
Sinan GENÇ	400420026	52876282752	Elektrik ve Bilgisayar Mühendisliği	Doktora	13/07/2023
Tezin Adı:	Optical Scattering Based Random Forest Assisted Particle Detection and Classification				
Danışmanı:	Doç. Dr. Kutay İÇÖZ				
II. Danışmanı:	Dr. Öğr. Üyesi Talha ERDEM				

ASLI GİBİDİR

Burhan KABATAŞ
Enstitü Sekreteri